



# First principles investigations of structural and optoelectronic properties of cubic $\text{Mg}_x\text{Zn}_{1-x}\text{Se}_y\text{Te}_{1-y}$ quaternary semiconductor alloys using FP-LAPW approach

Debankita Ghosh<sup>1</sup> · Sayantika Chanda<sup>1</sup> · Bimal Debnath<sup>1</sup> · Manish Debbarma<sup>1</sup> · Rahul Bhattacharjee<sup>1,2</sup> · Surya Chattopadhyaya<sup>1</sup>

Received: 28 May 2019 / Accepted: 14 August 2019 / Published online: 24 August 2019  
© Springer-Verlag GmbH Germany, part of Springer Nature 2019

## Abstract

Structural and optoelectronic properties of technologically important  $\text{Mg}_x\text{Zn}_{1-x}\text{Se}_y\text{Te}_{1-y}$  quaternary alloys are calculated employing DFT-based FP-LAPW approach. Computations of exchange–correlation potentials are performed with PBE-GGA for structural properties and both the mBJ and EV-GGA for optoelectronic properties. Each specimen within  $\text{Mg}_x\text{Zn}_{1-x}\text{Se}_y\text{Te}_{1-y}$  system is a direct band gap ( $\Gamma$ – $\Gamma$ ) semiconductor. At each cationic (Mg) concentration  $x$ , lattice constant decreases, while bulk modulus and band gap increase nonlinearly with increase in anionic (Se) concentration  $y$ . Again, nonlinear increase in lattice constant and band gap, while decrease in bulk modulus is observed with increase in cationic concentration  $x$  at each anionic concentrations  $y$ . Calculated band gap bowing for few ternary alloy systems are in good agreement with corresponding experimental data. The calculated contour maps for lattice constants and energy band gaps would be very useful for designing new quaternary alloys with desired optoelectronic properties. Optical properties of the said specimens within  $\text{Mg}_x\text{Zn}_{1-x}\text{Se}_y\text{Te}_{1-y}$  quaternary system show several interesting features. Composition dependence of each calculated zero-frequency limit shows opposite trend, while each calculated critical point shows similar trend of composition dependence of band gap. Finally, suitability of ZnTe and InAs as substrates for the growth of several zinc-blende  $\text{Mg}_x\text{Zn}_{1-x}\text{Se}_y\text{Te}_{1-y}$  quaternary alloys has been investigated.

## 1 Introduction

In materials science and engineering, optoelectronic and various other physical properties of semiconductors can be tuned by the alloy formation process for satisfactory fabrication of application-oriented semiconductor devices. Though the formation of ternary alloys is the introductory process, the possibility of formation of quaternary or multinary alloys provides us more capability of precise tuning of various physical properties of semiconductors to achieve the target

and hence widen their applications. The choice of suitable elemental or compound semiconductors with wider range of band gaps as ingredients and the fabrication procedure to ensure stable and low-resistive p-type doping, highly stable Ohmic contacts and low defect density in the fabricated ternary and quaternary alloys are very important in their efficient microelectronic and optoelectronic applications [1, 2].

Recently, ternary and quaternary semiconductor alloys, fabricated on the basis of II–VI compounds, are attracting enormous attraction due to their interesting optoelectronic properties in the visible and far-infrared spectral region [3–8]. The wide band gap diatomic zinc selenide (ZnSe) and zinc telluride (ZnTe) belong to IIB–VIA transition metal chalcogenide family, while magnesium selenide (MgSe) and magnesium telluride (MgTe) belong to the group IIA–VIA alkaline-earth chalcogenide family. The ZnSe are widely used in manufacturing blue-green laser diodes [9]. Moreover, both the ZnSe and ZnTe are used to prepare optical wave guides [10] and wide-band-gap hetero-structure lasers [11]. The MgSe and MgTe based hetero-junctions are also well known as wide band-gap light emitters [12].

**Electronic supplementary material** The online version of this article (<https://doi.org/10.1007/s00339-019-2938-5>) contains supplementary material, which is available to authorized users.

✉ Surya Chattopadhyaya  
surya\_ju@yahoo.com

- <sup>1</sup> Department of Physics, Tripura University, Suryamaninagar 799022, Tripura, India
- <sup>2</sup> Department of Physics, Women's College, Agartala 799001, Tripura, India

Under ambient conditions, both the ZnSe and ZnTe crystallized in cubic zinc blende (B3) or wurtzite (B4) phase [13] and exhibit high-pressure structural phase transition from zinc blende (B3) to rock-salt (B1) phase [14–16]. On the other hand, the ambient and most stable rock-salt structure for MgSe [17] and MgTe [18] was experimentally confirmed. Moreover, molecular beam epitaxial (MBE) growth of zinc blende MgSe [18] and MgTe [19] was also experimentally confirmed. Experimentally, MgSe exhibits the pressure-induced structural phase transition from rock-salt (B1) to iron silicide (B28) structure [17], while MgTe transforms from wurtzite (B4) to nickel-arsenide NiAs (B8) structure [18].

Several experimental studies on the electronic properties [20–24], optical properties [25, 26], elastic properties [27, 28] etc. on ZnSe and ZnTe have established their superiority in different areas of microelectronic and optoelectronic applications. In addition, the lattice parameters of zinc-blende MgSe [29, 30] and MgTe [24, 31] as well as rock-salt MgSe [17] and MgTe [18] were investigated. Experimental studies on their electronic properties indicate that ZnSe and ZnTe as well as MgSe and MgTe are wide direct fundamental band gap ( $\Gamma$ – $\Gamma$ ) semiconductors in their B3 phase [31, 32].

Experiments were performed for preparation and characterization of structural, morphological, electrical and optical properties of nano-crystalline cubic MgSe thin films [33, 34], molecular beam epitaxial (MBE) growth of ZnSe thin films and epilayers on GaAs substrates and their optical characterizations [35–37], molecular beam epitaxial (MBE) growth of cubic MgTe thin films as suitable materials for optoelectronic applications in the entire visible range [38]. Moreover, MBE growth of ZnTe epilayers on InAs substrates and their optical and structural characterizations [30], structural and optical characterizations of molecular beam epitaxially (MBE) grown ZnTe epilayers on GaAs substrates with ZnSe/ZnTe strained superlattices buffer layers [39], electrical characterizations of ZnTe thin films, deposited by thermal evaporation method on n-type Si substrate [40], studies of Raman spectroscopy and photoluminescence of molecular-beam epitaxially (MBE) grown ZnTe thin films on GaAs substrates [41], etc. have also been performed for their different potential applications.

Recently, bulk II–VI ternary and quaternary alloys as well as their thin films and nanostructures were investigated extensively to identify their suitable areas of microelectronic and optoelectronic applications. Some of the remarkable investigations include synthesis of ternary  $\text{ZnSe}_x\text{Te}_{1-x}$  alloy thin films by solid-state reactions and study of their structural, morphological and optical properties [42], deposition of  $\text{ZnSe}_{1-x}\text{Te}_x$  epilayers on GaAs substrates by isothermal closed space sublimation (ICSS) technique and their structural characterization [43], solution-phase synthesis of

$\text{ZnSe}_x\text{Te}_{1-x}$  ternary alloyed nanowires and investigations of their band gap bowing [44], etc. No experimental study on MgSeTe bulk ternary alloys as well as their thin films and nanostructures has yet been performed so far.

Several experiments on mixed magnesium–zinc–chalcogenide ternary alloys as well as their thin films performed so far include MBE growth of  $\text{Zn}_{1-x}\text{Mg}_x\text{Se}$  ternary alloys and measurement of their lattice constants and band gaps [29], MBE growth of  $\text{Mg}_x\text{Zn}_{1-x}\text{Se}$  ternary alloys on GaAs substrate and their visible–near ultraviolet spectroscopic ellipsometric (SE) studies on optical properties [45], high-pressure Bridgman growth of  $\text{Zn}_{1-x}\text{Mg}_x\text{Se}$  mixed crystals and Mg-concentration dependence of their lattice constants, luminescences and electrical properties [46], MBE growth of zinc-blende  $\text{Zn}_{1-x}\text{Mg}_x\text{Se}$  alloys on GaAs substrate and spectroscopic ellipsometric (SE) investigation of their optical properties at room temperature [47], photoluminescence (PL) measurements of band gaps, room temperature optical reflectivity and wavelength dependence of the refractive indices of MBE grown  $\text{Zn}_{1-x}\text{Mg}_x\text{Te}$  ternary wide-gap semiconductor alloys over a wide range of compositions [48], etc.

In case of magnesium–zinc–chalcogenides quaternary alloys, some experimental studies were also performed so far. Few of them include MBE growth of  $\text{Zn}_{1-x}\text{Mg}_x\text{Se}_y\text{Te}_{1-y}$  epilayers and  $\text{ZnTe}/\text{Zn}_{1-x}\text{Mg}_x\text{Se}_y\text{Te}_{1-y}$  quantum wells (QW) on InAs substrates and their structural, electronic and optical characterizations [30], MBE growth of quaternary alloys  $\text{Zn}_{1-x}\text{Mg}_x\text{Se}_y\text{Te}_{1-y}$  on InAs substrate and their structural characterizations [32], MBE growth of  $\text{Mg}_x\text{Zn}_{1-x}\text{Se}_y\text{Te}_{1-y}$  quaternary alloys on InP substrate and their structural, electronic and optical characterizations [49], MBE growth of  $\text{Zn}_{1-x}\text{Mg}_x\text{Se}_y\text{Te}_{1-y}$  alloys on ZnTe substrates and photoluminescence studies of their optical properties [50], etc.

On the theoretical side, structural properties and phase stabilities, high-pressure structural phase transition from B3 to B1 phase, phonon dispersions, elastic properties, band structures and electronic properties, optical properties, thermal and thermodynamic properties and lattice dynamics of bulk diatomic zinc blende ZnSe and ZnTe [51–63] as well as MgSe and MgTe [63–72] have been studied under the framework of different DFT-based approaches and taking into consideration a variety of exchange–correlation potential schemes.

In case of bulk pure zinc chalcogenide ternary alloys ZnSeTe and magnesium chalcogenide ternary alloys MgSeTe, few theoretical studies performed so far include calculations of origins of optical bowing for  $\text{ZnSe}_x\text{Te}_{1-x}$  alloys [73], self-consistent ab initio FP-LAPW investigation of the structural, electronic and thermodynamic properties of  $\text{ZnSe}_x\text{Te}_{1-x}$  semiconductor ternary alloys [74], first-principles study of structural, elastic and thermodynamic properties of  $\text{ZnSe}_x\text{Te}_{1-x}$  ternary alloys [75], DFT-based FP-LAPW investigation of structural, electronic and thermodynamic properties of zinc blende

MgSe<sub>x</sub>Te<sub>1-x</sub> ternary alloys [76], FP-LAPW investigation of electronic and optical properties of zinc blende MgSe<sub>x</sub>Te<sub>1-x</sub> ternary alloys [77].

In case of bulk magnesium–zinc chalcogenide mixed ternary alloys MgZnSe/Te, theoretical studies performed so far include DFT-based FP-LAPW investigations of structural and electronic properties of zinc-blende Zn<sub>1-x</sub>Mg<sub>x</sub>X (X=Se and Te) ternary alloys [78, 79], structural, electronic and optical properties of zinc-blende Zn<sub>1-x</sub>Mg<sub>x</sub>X (X=Se and Te) ternary alloys [80] as well as the structural and optoelectronic properties of zinc blende Mg<sub>x</sub>Zn<sub>1-x</sub>Te ternary alloys [81]. A couple of recent studies on ternary alloys with Mg or Zn as one of the constituents include FP-LAPW based investigations of the structural, electronic and optical properties of Mg<sub>x</sub>Cd<sub>1-x</sub>X [82] and Zn<sub>1-x</sub>Hg<sub>x</sub>X [83] (X=Se and Te).

In case of bulk magnesium–zinc–chalcogenides quaternary alloys MgZnSeTe, theoretical studies performed are rare in number and only a couple of studies have been performed so far. In the first study, Shim and coworkers [84] have utilized the correlated function expansion (CFE) methodology to calculate the energy band gap and the alloy bond length of Zn<sub>1-x</sub>Mg<sub>x</sub>Se<sub>y</sub>Te<sub>1-y</sub> quaternary alloys over the entire composition space ( $x, y$ ). In the subsequent study, Hassan and coworkers [85] have studied the structural and electronic properties of Zn<sub>1-x</sub>Mg<sub>x</sub>Se<sub>y</sub>Te<sub>1-y</sub> quaternary alloys using the DFT-based FP-LAPW approach. But these studies covered very inadequate number of compounds as well as properties so that a detailed theoretical study on various properties of all the compounds under the Mg<sub>x</sub>Zn<sub>1-x</sub>Se<sub>y</sub>Te<sub>1-y</sub> quaternary system with appropriate exchange–correlation (XC) functional is necessary for whole range of Mg-concentration ( $x$ ) and Se-concentration ( $y$ ).

In this paper, we have presented the results obtained from systematic theoretical study of structural, electronic and optical properties of cubic binary, ternary and quaternary specimens within the Mg<sub>x</sub>Zn<sub>1-x</sub>Se<sub>y</sub>Te<sub>1-y</sub> quaternary system for whole range of cationic ( $x$ ) and anionic ( $y$ ) concentrations ( $x, y = 0.0, 0.25, 0.50, 0.75$  and  $1.0$ ). First principle based FP-LAPW approach has been applied along with appropriate schemes for calculations of necessary XC functional for structural and optoelectronic properties. Moreover, we have made an elaborate study on the anionic (Se) concentration  $y$  and cationic (Mg) concentration  $x$  dependence of the said properties of the specimens within this quaternary system. Our calculated data will propose new experiments as well as suggest them as potential candidates in different optoelectronic applications.

## 2 Computational details

Density functional theory (DFT) [86, 87] based full-potential linearized augmented plane wave (FP-LAPW) methodology [88] has been efficiently implemented in WIEN2K

code [89, 90] and it has been used to carry out present study to compute structural, electronic and optical properties of binary, ternary and quaternary specimens under the Mg<sub>x</sub>Zn<sub>1-x</sub>Se<sub>y</sub>Te<sub>1-y</sub> quaternary system. For structural properties, the exchange–correlation (XC) potentials have been calculated with Perdew–Burke–Ernzerhof generalized gradient approximation (PBE-GGA) [91], while the modified Becke–Johnson (mBJ) [92, 93] and Engel–Vosko generalized gradient approximation (EV-GGA) [94] schemes have been utilized for efficient calculations of XC potentials for electronic and optical properties. For structure visualization purpose and to carry out some analysis, the graphic code XCrySDen [95] has been utilized in the present study.

In the FP-LAPW approach, Kohn–Sham wave functions inside the non-overlapping muffin-tin spheres, surrounding the atomic sites, have been expanded in spherical harmonics with the maximum value of angular momentum  $l_{\max} = 10$ . The same are expanded with plane waves basis set in the interstitial region of the unit cell with a cut-off value  $K_{\max} = 8.0/R_{\text{MT}}$ , where  $R_{\text{MT}}$  is the smallest muffin-tin radius and the  $K_{\max}$  is the magnitude of the largest  $K$ -vector in the plane wave expansion. The potential and charge density Fourier expansion parameter  $G_{\max}$  is taken as  $16 \text{ Ry}^{1/2}$ . The  $R_{\text{MT}}$  values of Mg, Zn, Se and Te are taken as 2.3, 2.5, 2.4 and 2.5 a.u., respectively. The Brillouin zone integrations have been performed using a mesh of 5000  $k$ -points. Both the plane wave cutoff and the number of  $k$ -points were varied to ensure total energy convergence and it is achieved through self-consistent-field (SCF) calculations with an energy threshold value of  $10^{-5} \text{ Ry}$ .

The Mg<sub>x</sub>Zn<sub>1-x</sub>Se<sub>y</sub>Te<sub>1-y</sub> quaternary alloy system is surrounded by two cationic ternary alloy systems Mg<sub>x</sub>Zn<sub>1-x</sub>Se and Mg<sub>x</sub>Zn<sub>1-x</sub>Te as well as two anionic ternary alloy systems ZnSe<sub>y</sub>Te<sub>1-y</sub> and MgSe<sub>y</sub>Te<sub>1-y</sub>. They, in turn, formed from the four binary compounds ZnSe, ZnTe, MgSe and MgTe. Therefore, in the introductory stage, we have adopted the eight-atom  $1 \times 1 \times 1$  cubic zinc-blende unit cell of these binary compounds in our calculations. These have been designed by using the experimental lattice parameters of ZnSe [21], ZnTe [21], MgSe [32] and MgTe [32]. The anionic ternary alloys ZnSe<sub>y</sub>Te<sub>1-y</sub> and MgSe<sub>y</sub>Te<sub>1-y</sub> at  $y = 0.25, 0.50$  and  $0.75$  have been designed by successive substitution of Te atom(s) with Se atom(s) in the  $1 \times 1 \times 1$  unit cell of ZnTe and MgTe, respectively. The cationic ternary alloys Mg<sub>x</sub>Zn<sub>1-x</sub>Se and Mg<sub>x</sub>Zn<sub>1-x</sub>Te at  $x = 0.25, 0.50$  and  $0.75$  have been designed by successive replacement of Zn atom(s) with Mg atom(s) in  $1 \times 1 \times 1$  unit cell of ZnSe and ZnTe, respectively. Each of the ternary alloys for  $x/y = 0.25, 0.50$  and  $0.75$  is a simple eight-atom cubic cell. The quaternary (pseudo ternary) alloys Mg<sub>x</sub>Zn<sub>1-x</sub>Se<sub>y</sub>Te<sub>1-y</sub> for  $x = 0.25, 0.50$  and  $0.75$  have been designed by cationic substitution process i.e. consecutive substitution of Zn atom(s) with Mg atom(s) in the cubic unit cells of anionic ternary alloys ZnSe<sub>y</sub>Te<sub>1-y</sub>

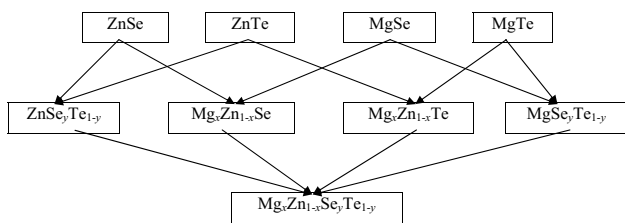


**Fig. 1** Schematic diagram for formation of ternary and quaternary alloys within  $\text{Mg}_x\text{Zn}_{1-x}\text{Se}_y\text{Te}_{1-y}$  system from their basic constituent binary compounds

( $y=0.25, 0.50$  and  $0.75$ ) and each of the resultant quaternary structures is also an eight-atom cubic cell. They can also be formed from the other three ternary systems by cationic/anionic substitution process. The schematic diagram of the procedure of formation of ternary and quaternary alloys from their basic constituent binaries [96] is presented as Fig. 1. The crystal structures of newly designed nine cubic quaternary specimens within  $\text{Mg}_{0.25}\text{Zn}_{0.75}\text{Se}_y\text{Te}_{1-y}$ ,  $\text{Mg}_{0.50}\text{Zn}_{0.50}\text{Se}_y\text{Te}_{1-y}$ , and  $\text{Mg}_{0.75}\text{Zn}_{0.25}\text{Se}_y\text{Te}_{1-y}$  systems are presented in Figs. S1a–c, S2a–c and S3a–c, respectively for  $y=0.25, 0.50$  and  $0.75$  in the Supplementary Materials.

In the present study, the concentration dependence of structural, electronic and optical properties has been investigated by considering the  $\text{Mg}_x\text{Zn}_{1-x}\text{Se}_y\text{Te}_{1-y}$  quaternary system into five sub-systems on the basis of variation of  $x$  and  $y$  in two ways. In the first way, we have considered the entire anionic concentration range  $y=0.0, 0.25, 0.50, 0.75$  and  $1.0$  at each of the five cationic concentrations  $x=0.0, 0.25, 0.50, 0.75$  and  $1.0$  and investigated the effects of successive anionic substitution on these properties at each of the cationic concentrations. In the second way, we have taken the entire cationic concentration range  $x=0.0, 0.25, 0.50, 0.75$  and  $1.0$  at each of the five anionic concentrations  $y=0.0, 0.25, 0.50, 0.75$  and  $1.0$  and investigated the effects of successive cationic substitution on the aforesaid properties at each of the anionic concentrations. In both the ways, the qualitative nature of specimens in each sub-system, formed at either fixed  $x$  or  $y$ , is similar and they are presented in terms of a matrix in Table 1.

## 3 Results and discussions

### 3.1 Structural properties

The structural properties of the binary, ternary and quaternary specimens within the  $\text{Mg}_x\text{Zn}_{1-x}\text{Se}_y\text{Te}_{1-y}$  quaternary system have been computed using structural optimization technique, where the total energy of each of the designed unit cells is minimized with respect to the cell parameters as well as atomic positions. The total energies of each unit

**Table 1** Matrix for qualitative nature of specimen for different  $x$  and  $y$

$x$	$y$				
	0.0	0.25	0.50	0.75	1.0
0.0	B	T	T	T	B
0.25	T	Q	Q	Q	T
0.50	T	Q	Q	Q	T
0.75	T	Q	Q	Q	T
1.0	B	T	T	T	B

*B* binary, *T* ternary, *Q* quaternary

cell at different volumes, around the equilibrium unit cell volume, are calculated using the self-consistent-field (SCF) technique and the resultant parabolic variation is fitted to Murnaghan's equation of state [97]. From such fitting, we have achieved the ground-state structural parameters, such as minimum energy ( $E_0$ ), equilibrium volume ( $V_0$ ), equilibrium lattice parameter ( $a_0$ ), bulk modulus ( $B_0$ ) and first-order pressure derivative of bulk modulus ( $B'_0$ ) for each sample, as presented in Table 2. Also, some available experimental and earlier theoretical structural data for the specimens are also included in Table 2 for comparison.

#### 3.1.1 Lattice constant and bulk modulus of binary, ternary and quaternary specimens

For binary compounds ZnSe and ZnTe, our computed structural data have been compared with some available experimental  $a_0$ ,  $B_0$  and  $B'_0$  data [20, 21, 27]. Our computed  $a_0$  and  $B_0$  for ZnSe and ZnTe agree well with the respective experimental data, though the computed  $a_0$  for both specimens are marginally overestimated and  $B_0$  is marginally underestimated with respect to the corresponding reported experimental data. In case of  $B'_0$ , our computed data for ZnSe and ZnTe are underestimated by 0.497 and 0.029, respectively, compared to the corresponding experimental data [20, 27]. In case of other pair of binary compounds MgSe and MgTe, only equilibrium lattice constant  $a_0$  is reported from several experimental observations [29, 30, 32, 48], while none of their experimental  $B_0$  and  $B'_0$  data are available for comparison. In each case, our calculated  $a_0$  agrees excellently well with the corresponding experimental data, though each of them is marginally overestimated with respect to the corresponding reported experimental findings.

In the present study, we have also compared our computed  $a_0$ ,  $B_0$  and  $B'_0$  data for the said binary compounds with some available data obtained from some earlier theoretical calculations for ZnSe and ZnTe [54–60, 62, 79–81] as well as MgSe and MgTe [64–67, 67, 71, 76, 79–81]. Our computed  $a_0$  and  $B_0$  for ZnSe, ZnTe, MgSe and MgTe are in good agreement with several corresponding earlier theoretical data. Moreover, our calculated  $a_0$  data for the binary compounds ZnSe,

**Table 2** Calculated  $a_0$ ,  $B_0$  and  $B'/$  of binary, ternary and quaternary specimens within  $Mg_xZn_{1-x}Se_yTe_{1-y}$  system

$x$	$y$	Specimen	$a_0$ (Å)	$B_0$ (GPa)	$B'/$
0.0	0.0	ZnTe	6.104	48.56	5.011
			6.089 <sup>a</sup> , 6.1037 <sup>b</sup>	50.9 <sup>b</sup>	5.04 <sup>b</sup>
			6.020 <sup>a1</sup> , 6.174 <sup>b1</sup> , 6.103 <sup>c1</sup> , 6.063 <sup>d1</sup> , 6.00 <sup>e1</sup> , 6.11 <sup>a3</sup> , 6.10 <sup>b3</sup> , 6.198 <sup>c3</sup>	49.2 <sup>a1</sup> , 51.2 <sup>b1</sup> , 52.9 <sup>c1</sup> , 50.54 <sup>d1</sup> , 55.21 <sup>e1</sup> , 50.18 <sup>a3</sup> , 45.94 <sup>b3</sup> , 44.35 <sup>c3</sup>	4.88 <sup>b1</sup> , 4.60 <sup>e1</sup>
			6.087	50.96	4.501
			6.099 <sup>a2</sup>	45.63 <sup>a2</sup>	
0.25	0.25	ZnSe <sub>0.25</sub> Te <sub>0.75</sub>	5.979	52.71	4.747
			5.989 <sup>a2</sup>	48.90 <sup>a2</sup>	
0.50	0.50	ZnSe <sub>0.50</sub> Te <sub>0.50</sub>	5.861	55.18	5.165
			5.873 <sup>a2</sup>	52.14 <sup>a2</sup>	
0.75	0.75	ZnSe <sub>0.75</sub> Te <sub>0.25</sub>	5.674	60.08	4.273
			5.669 <sup>a</sup> , 5.67 <sup>b</sup> , 5.667 <sup>c</sup>	62.5 <sup>b</sup> , 64.7 <sup>c</sup>	4.77 <sup>c</sup>
			5.630 <sup>f1</sup> , 5.582 <sup>g1</sup> , 5.618 <sup>h1</sup> , 5.66 <sup>a3</sup> , 5.738 <sup>c3</sup>	63.34 <sup>f1</sup> , 70.8 <sup>g1</sup> , 67.6 <sup>h1</sup> , 82.26 <sup>a3</sup> , 58.20 <sup>c3</sup>	4.57 <sup>i1</sup>
0.25	0.0	Mg <sub>0.25</sub> Zn <sub>0.75</sub> Te	6.198	44.62	4.871
			6.20 <sup>a3</sup> , 6.18 <sup>b3</sup> , 6.284 <sup>c3</sup>	46.26 <sup>a3</sup> , 34.95 <sup>b3</sup> , 40.79 <sup>c3</sup>	
			6.177	46.23	4.365
			6.064	48.81	4.629
			5.942	50.86	5.011
0.50	0.0	Mg <sub>0.50</sub> Zn <sub>0.50</sub> Te	5.803	52.69	4.035
			5.72 <sup>a3</sup> , 5.815 <sup>c3</sup>	74.15 <sup>a3</sup> , 52.96 <sup>c3</sup>	
0.50	0.25	Mg <sub>0.50</sub> Zn <sub>0.50</sub> Se <sub>0.25</sub> Te <sub>0.75</sub>	6.359	37.85	4.127
			6.275 <sup>a3</sup> , 6.27 <sup>b3</sup> , 6.363 <sup>c3</sup>	41.14 <sup>a3</sup> , 37.48 <sup>b3</sup> , 37.4 <sup>c3</sup>	
			6.257	39.95	4.098
			6.141	41.06	4.316
			5.993	44.36	6.427
0.75	0.25	Mg <sub>0.75</sub> Zn <sub>0.25</sub> Se <sub>0.75</sub> Te <sub>0.25</sub>	5.873	50.03	4.033
			5.80 <sup>a3</sup> , 5.877 <sup>c3</sup>	66.35 <sup>a3</sup> , 49.18 <sup>c3</sup>	
0.75	0.0	Mg <sub>0.75</sub> Zn <sub>0.25</sub> Te	6.384	35.21	3.792
			6.35 <sup>a3</sup> , 6.36 <sup>b3</sup> , 6.442 <sup>c3</sup>	39.37 <sup>a3</sup> , 39.94 <sup>b3</sup> , 35.09 <sup>c3</sup>	
			6.333	37.38	3.862
			6.214	39.12	4.049
			6.082	42.88	4.314
1.0	0.0	MgTe	5.935	48.14	3.653
			5.86 <sup>a3</sup> , 5.938 <sup>c3</sup>	63.94 <sup>a3</sup> , 47.99 <sup>c3</sup>	
			6.427	33.54	3.672
0.25	0.25	MgSe <sub>0.25</sub> Te <sub>0.75</sub>	6.42 <sup>d</sup> , 6.35 <sup>e</sup> , 6.42 <sup>f</sup>		
			6.39 <sup>i1</sup> , 6.38 <sup>j1</sup> , 6.4454 <sup>k1</sup> , 6.512 <sup>l1</sup> , 6.517 <sup>b2</sup> , 6.43 <sup>a3</sup> , 6.517 <sup>b3</sup> , 6.517 <sup>c3</sup>	38.0 <sup>i1</sup> , 38.7 <sup>j1</sup> , 38.0 <sup>k1</sup> , 33.52 <sup>l1</sup> , 33.97 <sup>b2</sup> , 34.85 <sup>a3</sup> , 33.70 <sup>c3</sup>	3.79 <sup>i1</sup> , 3.89 <sup>j1</sup> , 3.96 <sup>k1</sup> , 4.604 <sup>l1</sup>
			6.403	35.37	3.732
			6.407 <sup>b2</sup>	36.02 <sup>b2</sup>	
			6.279	37.04	3.913
0.50	0.50	MgSe <sub>0.50</sub> Te <sub>0.50</sub>	6.283 <sup>b2</sup>	38.43 <sup>b2</sup>	
			6.144	40.48	3.942
0.75	0.75	MgSe <sub>0.75</sub> Te <sub>0.25</sub>	6.148 <sup>b2</sup>	41.21 <sup>b2</sup>	
			5.995	46.34	3.525
1.0	0.0	MgSe	5.89 <sup>d, h</sup> , 5.91 <sup>g</sup>		
			5.92 <sup>i1</sup> , 5.87 <sup>j1</sup> , 5.99 <sup>m1</sup> , 6.005 <sup>b2</sup> , 5.93 <sup>a3</sup> , 6.002 <sup>c3</sup>	49.0 <sup>i1</sup> , 50.5 <sup>j1</sup> , 45.3 <sup>m1</sup> , 45.12 <sup>b2</sup> , 57.81 <sup>a3</sup> , 44.48 <sup>c3</sup>	

Experimental data: <sup>a</sup>Ref. [21], <sup>b</sup>Ref. [20], <sup>c</sup>Ref. [27], <sup>d</sup>Ref. [32], <sup>e</sup>Ref.[30], <sup>f</sup>Ref. [48], <sup>g</sup>Ref. [29], <sup>h</sup>Ref. [19]. Earlier theoretical data: <sup>a1</sup>Ref. [54], <sup>b1</sup>Ref. [55], <sup>c1</sup>Ref. [56], <sup>d1</sup>Ref.[58], <sup>e1</sup>Ref. [59], <sup>f1</sup>Ref. [60], <sup>g1</sup>Ref. [62], <sup>h1</sup>Ref. [57], <sup>i1</sup>Ref.[66], <sup>j1</sup>Ref. [65], <sup>k1</sup>Ref. [64], <sup>l1</sup>Ref. [71], <sup>m1</sup>Ref. [67], <sup>a2</sup>Ref. [74], <sup>b2</sup>Ref. [76], <sup>a3</sup>Ref. [80], <sup>b3</sup>Ref.[81], <sup>c3</sup>Ref. [79]



ZnTe, MgSe and MgTe show best agreement with some of the corresponding experimental outcomes relative to all of the reported other theoretical findings.

Any experimental structural data for the anionic ternary alloys  $\text{ZnSe}_y\text{Te}_{1-y}$  and  $\text{MgSe}_y\text{Te}_{1-y}$ , as well as cationic ternary alloys  $\text{Mg}_x\text{Zn}_{1-x}\text{Se}$  and  $\text{Mg}_x\text{Zn}_{1-x}\text{Te}$  are unavailable for comparison. But, earlier theoretical  $a_0$  and  $B_0$  data for  $\text{ZnS}_y\text{Se}_{1-y}$  [74],  $\text{MgS}_y\text{Te}_{1-y}$  [76],  $\text{Mg}_x\text{Zn}_{1-x}\text{Se}$  [79, 80] and  $\text{Mg}_x\text{Zn}_{1-x}\text{Te}$  [79–81] ternary alloys are available for comparison. The calculated  $a_0$  for each of the anionic ternary alloys  $\text{ZnSe}_y\text{Te}_{1-y}$  is marginally underestimated, while  $B_0$  for each of them is marginally overestimated with respect to the corresponding earlier theoretical data [74]. In case of each of the other anionic ternary alloys  $\text{MgSe}_y\text{Te}_{1-y}$ , both of our calculated  $a_0$  and  $B_0$  are marginally underestimated with respect to the corresponding earlier theoretical data [76]. In case of cationic ternary specimens within  $\text{Mg}_x\text{Zn}_{1-x}\text{Se}$  and  $\text{Mg}_x\text{Zn}_{1-x}\text{Te}$  systems, both of our calculated  $a_0$  and  $B_0$  for each specimen are in excellent agreement with most of the corresponding earlier theoretical data [79–81].

In case of quaternary specimens within the  $\text{Mg}_x\text{Zn}_{1-x}\text{Se}_y\text{Te}_{1-y}$  system, we are unable to compare our computed structural data due to lack of such kind of experimental or earlier theoretical data in literature.

### 3.1.2 Concentration dependence of lattice constant and bulk modulus

In the present study, we have investigated the concentration dependence of  $a_0$  and  $B_0$  for the specimens within the  $\text{Mg}_x\text{Zn}_{1-x}\text{Se}_y\text{Te}_{1-y}$  quaternary system for the entire cationic and anionic concentration range  $x/y=0.0, 0.25, 0.50, 0.75$  and  $1.0$ . Keeping the cationic (Mg) concentration  $x$  fixed at each of the five specified values, we have observed that the  $a_0$  decreases with increase in anionic (Se) concentration  $y$  and each of such variations is presented in Fig. 2a. In this case, substitution of tellurium atom(s) of higher radius ( $1.23 \text{ \AA}$ ) with selenium atom(s) of lower radius ( $1.03 \text{ \AA}$ ) decreases the volume of the cubic unit cell and hence the lattice constant  $a_0$ . Due to inversely proportional relationship between lattice constant and bulk modulus, we have observed increment in  $B_0$  with increase in anionic (Se) concentration  $y$  at each of the five aforesaid cationic concentrations  $x$ , presented in Fig. 2b.

Again, keeping the anionic (Se) concentration  $y$  fixed at each of the five specific values, we have observed that  $a_0$  increases with increase in cationic (Mg) concentration  $x$  and each of such variations is presented in Fig. 2c. The substitution of zinc atom(s) of lower radius ( $1.42 \text{ \AA}$ ) with magnesium atom(s) of slightly higher radius ( $1.45 \text{ \AA}$ ) is responsible for the increase in cubic unit cell volume and hence  $a_0$ . This, in turn, decreases the  $B_0$  with increase in cationic (Mg)

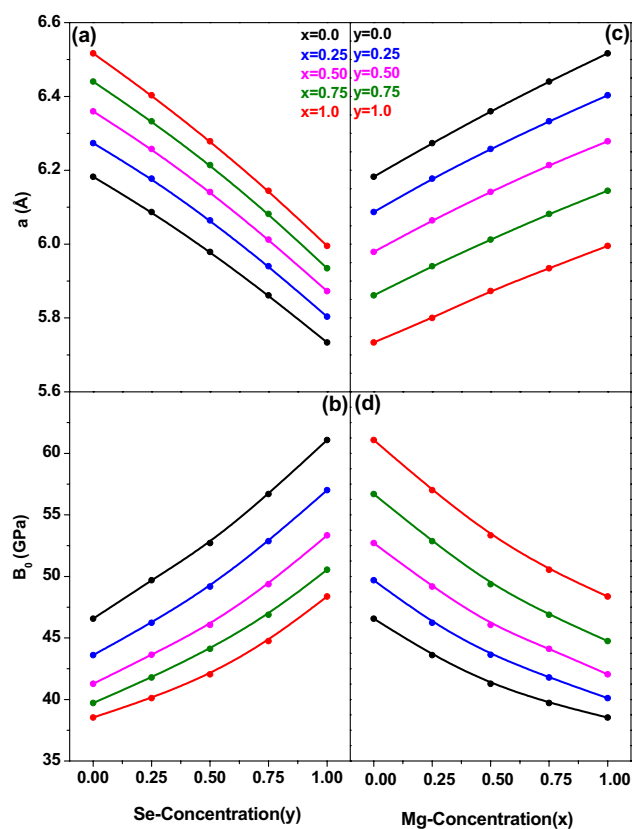


**Fig. 2** Variations of calculated  $a_0$  with Se-concentration  $y$  at each of the fixed Mg-concentrations  $x$ ,  $b$   $B_0$  with Se-concentration  $y$  at each of the fixed Mg-concentrations  $x$ ,  $c$   $a_0$  with Mg-concentration  $x$  at each of the fixed Se-concentrations  $y$ ,  $d$   $B_0$  with Mg-concentration  $x$  at each of the fixed Se-concentrations  $y$  of the specimens within  $\text{Mg}_x\text{Zn}_{1-x}\text{Se}_y\text{Te}_{1-y}$  quaternary system

concentration  $x$  at each of the five aforesaid anionic (Se) concentrations  $y$  and such variations are presented in Fig. 2d.

It is also observed from Fig. 2b that at any specific selenium concentration  $y$ , bulk modulus and hence the hardness of the specimen gradually decreases with increase in Mg-concentration  $x$  in the unit cell. Moreover, it is observed from Figs. 2d that at any specific Mg-concentration  $x$ , the hardness of the specimen gradually increases with increase in selenium concentration  $y$  in the unit cell.

From Fig. 2a, b, we have observed nonlinear variation of  $a_0$  and  $B_0$ , respectively, with selenium concentration  $y$  at each of the magnesium concentrations  $x$ . Also, the variation of  $a_0$  and  $B_0$  with magnesium concentration  $x$  at each of the selenium concentrations  $y$ , shown in Fig. 2c, d, respectively, exhibits nonlinearity.

For an ideal alloy system, Vegard's law [98] suggests the linear concentration ( $x/y$ ) dependence (LCD) of lattice constant ( $a_0$ ), while experimental studies [29, 99] confirm a nonlinear variation in a real alloy system having the following form:

$$a(x) = \alpha_a + \beta_a x + \delta_a x^2 \tag{1}$$

The nonlinear coefficient  $\delta_a$  is the bowing parameter in lattice constant versus concentration curve for any real alloy system, which is obtained by fitting the corresponding  $a_0$  versus concentration ( $x/y$ ) curve with Eq. 1. Similar quadratic relationship is also valid to explain the nonlinear concentration dependence of bulk modulus in any real alloy system and the nonlinear coefficient  $\delta_B$  measures the bowing in bulk modulus versus concentration curve.

Now at each of the cationic concentrations  $x$ , the  $a_0$  versus  $y$  curve shows marginal upward bowing due to marginal mismatches between the lattice constants of the terminal binary/ternary compounds. The same is also observed in case of  $a_0$  versus  $x$  curve at each of the anionic concentrations  $y$ . Each of the  $B_0$  versus  $y$  as well as  $B_0$  versus  $x$  curves at each of the fixed  $x$  and  $y$ , respectively, shows small downward bowing due to small mismatch of the bulk modulus of the corresponding terminal binary/ternary compounds. In case of lattice constant as well as bulk modulus versus anionic/cationic concentration curves, the respective calculated bowing parameters  $\delta_a$  and  $\delta_B$  are presented in Table 3. It is observed from Table 3 that  $\delta_a$  increases, while  $\delta_B$  decreases gradually, as we proceed from  $ZnSe_yTe_{1-y}$  to  $MgSe_yTe_{1-y}$  by replacing consecutively Zn with Mg atom(s). On the other hand,  $\delta_a$  decreases, while  $\delta_B$  increases gradually as we proceed from  $Mg_xZn_{1-x}Te$  to  $Mg_xZn_{1-x}Se$  by replacing consecutively Te with Se atom(s).

The Contour map of each of the calculated lattice constant and bulk modulus versus the compositions  $x$  and  $y$  for  $Mg_xZn_{1-x}Se_yTe_{1-y}$  quaternary system are presented in Fig. 3a, b, where we again observe a marginal deviation of the lattice constant and bulk modulus from their respective LCD. If lattice constants or bulk modulus of four binary compounds are known, any one of them for ternary or

quaternary specimen, formed at any  $x$  and  $y$  in the range  $0 \leq x, y \leq 1$ , can be evaluated from the corresponding contour plot.

### 3.2 Electronic properties

Before applying any semiconductor in fabricating an electronic device, it is necessary to study its electronic properties, especially band gap, experimentally or theoretically in order to investigate its appropriateness in such fabrication process. In the present work, the electronic properties of the binary, ternary and quaternary specimens under the  $Mg_xZn_{1-x}Se_yTe_{1-y}$  quaternary system have been computed with mBJ and EV-GGA functional. The calculated band

**Table 3** Calculated bowing parameters from concentration dependence curves of  $a_0$  and  $B_0$

Alloy system	Fixed concentration	Variable concentration	$\delta_a$ (Å)	$\delta_B$ (GPa)
$ZnSe_yTe_{1-y}$	$x$	$y$	- 0.039	6.584
$Mg_{0.25}Zn_{0.75}Se_yTe_{1-y}$	$x$	$y$	- 0.041	5.897
$Mg_{0.50}Zn_{0.50}Se_yTe_{1-y}$	$x$	$y$	- 0.047	5.192
$Mg_{0.75}Zn_{0.25}Se_yTe_{1-y}$	$x$	$y$	- 0.053	4.514
$MgSe_yTe_{1-y}$	$x$	$y$	- 0.058	4.007
$Mg_xZn_{1-x}Te$	$y$	$x$	- 0.063	3.429
$Mg_xZn_{1-x}Se_{0.25}Te_{0.75}$	$y$	$x$	- 0.055	4.927
$Mg_xZn_{1-x}Se_{0.50}Te_{0.50}$	$y$	$x$	- 0.039	5.751
$Mg_xZn_{1-x}Se_{0.75}Te_{0.25}$	$y$	$x$	- 0.027	6.248
$Mg_xZn_{1-x}Se$	$y$	$x$	- 0.019	7.843

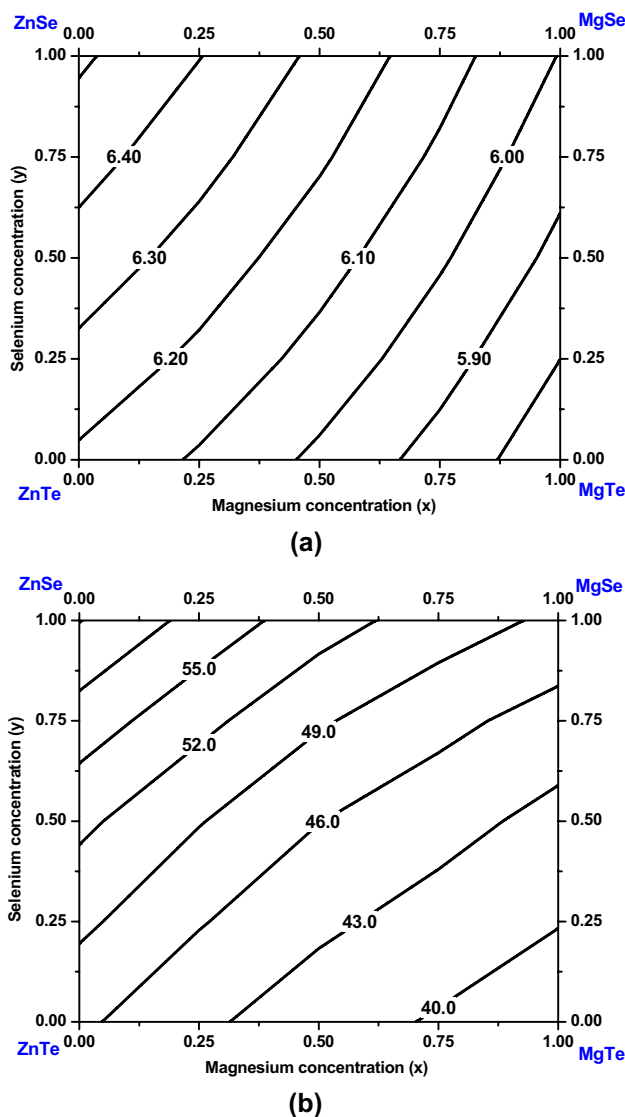


**Fig. 3** Contour map of the calculated **a** lattice constant  $a_0$ , **b** bulk modulus  $B_0$  versus the compositions  $x$  and  $y$  for  $Mg_xZn_{1-x}Se_yTe_{1-y}$  quaternary alloys

gaps for the compounds with both these XC functional are presented in Table 4 along with some available experimental as well as some earlier theoretical band gaps for comparison. It is observed from Table 4 that in case of each of the specimens under consideration, calculated band gap follows the trend  $E_g^{\text{mBJ}} > E_g^{\text{EV-GGA}}$  for the two XC functional used.

### 3.2.1 Band structures

The computed band structure of each of the binary compounds ZnSe, ZnTe, MgSe and MgTe indicates a direct minimum band gap ( $\Gamma$ - $\Gamma$ ) in their zinc-blende (B3) phase under both the XC functional used. Some experimental observations for ZnSe and ZnTe [20, 22] as well as MgSe and MgTe [24, 29–32] also support such qualitative features of the respective calculated band structures. The cubic ternary specimens within the  $\text{ZnSe}_y\text{Te}_{1-y}$ ,  $\text{MgSe}_y\text{Te}_{1-y}$ ,  $\text{Mg}_x\text{Zn}_{1-x}\text{Te}$  and  $\text{Mg}_x\text{Zn}_{1-x}\text{Se}$  systems also indicate a direct minimum band gap ( $\Gamma$ - $\Gamma$ ). Though any experimental information regarding the band structures of these specimens are not available, such feature of band structure of each of these ternary alloys has been confirmed by some respective earlier theoretical findings for  $\text{ZnSe}_y\text{Te}_{1-y}$  [73],  $\text{MgSe}_y\text{Te}_{1-y}$  [75],  $\text{Mg}_x\text{Zn}_{1-x}\text{Te}$  and  $\text{Mg}_x\text{Zn}_{1-x}\text{Se}$  [79, 80]. In case of band structure of each of the nine cubic quaternary specimens within the  $\text{Mg}_x\text{Zn}_{1-x}\text{Se}_y\text{Te}_{1-y}$  system, we have also observed direct band gap ( $\Gamma$ - $\Gamma$ ), but such qualitative feature cannot be compared due to unavailability of any experimental observation or earlier theoretical study of this kind. Such newly designed direct-band-gap and optically active semiconductor quaternary specimens may be useful in manufacturing faster and highly efficient optoelectronic devices [100]. The band structures of nine quaternary specimens within  $\text{Mg}_{0.25}\text{Zn}_{0.75}\text{Se}_y\text{Te}_{1-y}$ ,  $\text{Mg}_{0.50}\text{Zn}_{0.50}\text{Se}_y\text{Te}_{1-y}$  and  $\text{Mg}_{0.75}\text{Zn}_{0.25}\text{Se}_y\text{Te}_{1-y}$  systems are presented in Figs. S4a–c, S5a–c and S6a–c, respectively, for  $y = 0.25, 0.50$  and  $0.75$  in the Supplementary Materials.

### 3.2.2 Band gaps of binary, ternary and quaternary specimens

From Table 4, we have observed that our mBJ-based calculated band gap ( $E_g$ ) for each of the ZnSe and ZnTe is in excellent agreement with corresponding experimental data [20, 22], while the same with EV-GGA are much smaller than the corresponding experimental outcomes. On the other hand, our calculated band gap for MgSe with mBJ functional is 0.189 eV larger than a corresponding experimental data [29], while it is 0.589 eV larger than another corresponding experimental data [24]. Our EV-GGA based calculated band gap for MgSe lies between two reported experimental band gap data [24, 29]. Several experimental band gap data have been reported for MgTe [30–32]. Our mBJ-based calculated

band gap for MgTe is fairly overestimated with respect to each of the aforesaid experimental data. On the other hand, our computed EV-GGA based band gap for MgTe is in excellent agreement with one of the reported experimental band gap data [32], though our one is marginally underestimated by 0.046 eV.

It is to be noted that our mBJ-based calculated band gaps for ZnSe and ZnTe come closest to the corresponding experiment compared to the reported earlier theoretical data. Only a set of mBJ-based earlier theoretical band gap data for ZnSe and ZnTe [75] agree well with our respective mBJ-based calculated data, though they are 0.059 eV and 0.044 eV smaller compared to our respective mBJ-based computed data. In case of MgSe and MgTe, our computed band gap with mBJ functional is overestimated by 0.039 eV and 0.027 eV, respectively, compared to corresponding mBJ-based earlier theoretical data [80]. Some earlier theoretical EV-GGA based data for MgSe [75, 79, 80] and MgTe [71, 80] agree well with our corresponding calculated data with same XC functional.

It is to be noted that no experimental band gap data for any of the ternary alloys are available in literature for comparison. In case of each of the anionic ternary specimens, comparison of our calculated band gaps with different XC functional have been made with PBE-GGA and EV-GGA based earlier theoretical data for the corresponding ternary alloys within  $\text{ZnSe}_y\text{Te}_{1-y}$  [73] and  $\text{MgSe}_y\text{Te}_{1-y}$  [75] systems. Both of our mBJ- and EV-GGA based calculated band gaps for each of the anionic ternary specimens within  $\text{ZnSe}_y\text{Te}_{1-y}$  and  $\text{MgSe}_y\text{Te}_{1-y}$  systems are overestimated substantially with respect to each of the corresponding EV-GGA and PBE-GGA based earlier theoretical data [73, 75]. In case of all the cationic ternary specimens within the  $\text{Mg}_x\text{Zn}_{1-x}\text{Te}$  and  $\text{Mg}_x\text{Zn}_{1-x}\text{Se}$  systems, comparison of our calculated band gaps with different XC functional has been made mainly with some mBJ [80] and EV-GGA [79, 80] based corresponding earlier theoretical data. Our mBJ-based calculated band gap is overestimated for  $\text{Mg}_{0.25}\text{Zn}_{0.75}\text{Te}$ ,  $\text{Mg}_{0.50}\text{Zn}_{0.50}\text{Te}$  and  $\text{Mg}_{0.75}\text{Zn}_{0.25}\text{Te}$  by 0.154, 0.141 and 0.135 eV, respectively, and for  $\text{Mg}_{0.25}\text{Zn}_{0.75}\text{Se}$ ,  $\text{Mg}_{0.50}\text{Zn}_{0.50}\text{Se}$  and  $\text{Mg}_{0.75}\text{Zn}_{0.25}\text{Se}$  by 0.121, 0.339 and 0.266 eV, respectively, compared to the corresponding mBJ-based earlier theoretical data [75]. Our calculated band gap for each of the  $\text{Mg}_x\text{Zn}_{1-x}\text{Te}$  ternary alloys with EV-GGA functional is overestimated with respect to some corresponding earlier theoretical data [79, 80] with same XC functional. The same for each of the  $\text{Mg}_x\text{Zn}_{1-x}\text{Se}$  ternary alloys is marginally underestimated with respect to a set of corresponding earlier theoretical data [80], while marginally overestimated with respect to another set of corresponding earlier theoretical data [79], computed with same XC functional.

In case of any of the nine cubic quaternary specimens within  $\text{Mg}_x\text{Zn}_{1-x}\text{Se}_y\text{Te}_{1-y}$  system, no experimental or earlier



**Table 4** Calculated minimum band gaps of binary, ternary and quaternary specimens within  $Mg_xZn_{1-x}Se_yTe_{1-y}$  quaternary system using mBJ and EV-GGA functional

x	y	Specimen	Minimum energy band gap (eV)	
			EV-GGA	mBJ
0.0	0.0	ZnTe	1.821 2.39 <sup>a, b</sup> 1.33 <sup>a1%</sup> , 2.57 <sup>a1&amp;</sup> , 2.27 <sup>b1</sup> , 2.398 <sup>c1</sup> , 1.021 <sup>a2*</sup> , 1.577 <sup>a2#</sup> , 1.12 <sup>a3@</sup> , 1.76 <sup>a3#</sup> , 2.35 <sup>a3\$</sup> , 1.012 <sup>b3*</sup> , 1.575 <sup>b3#</sup>	2.394
		ZnSe <sub>0.25</sub> Te <sub>0.75</sub>	1.893 0.862 <sup>a2*</sup> , 1.457 <sup>a2#</sup>	2.421
		ZnSe <sub>0.50</sub> Te <sub>0.50</sub>	1.978 0.835 <sup>a2*</sup> , 1.448 <sup>a2#</sup>	2.529
		ZnSe <sub>0.75</sub> Te <sub>0.25</sub>	2.057 0.906 <sup>a2*</sup> , 1.545 <sup>a2#</sup>	2.644
		ZnSe	2.133 2.87 <sup>a</sup> , 2.82 <sup>b</sup> 1.45 <sup>a1%</sup> , 2.54 <sup>a1&amp;</sup> , 2.68 <sup>b1</sup> , 2.7 <sup>d1</sup> , 1.109 <sup>a2*</sup> , 1.863 <sup>a2#</sup> , 1.14 <sup>a3@</sup> , 2.09 <sup>a3#</sup> , 2.77 <sup>a3\$</sup> , 1.129 <sup>b3*</sup> , 1.889 <sup>b3#</sup>	2.829
0.25	0.0	Mg <sub>0.25</sub> Zn <sub>0.75</sub> Te	2.278 1.27 <sup>a3@</sup> , 1.91 <sup>a3#</sup> , 2.48 <sup>a3\$</sup> , 1.253 <sup>b3*</sup> , 1.827 <sup>b3#</sup>	2.634
		Mg <sub>0.25</sub> Zn <sub>0.75</sub> Se <sub>0.25</sub> Te <sub>0.75</sub>	2.345	2.718
		Mg <sub>0.25</sub> Zn <sub>0.75</sub> Se <sub>0.50</sub> Te <sub>0.50</sub>	2.438	2.806
		Mg <sub>0.25</sub> Zn <sub>0.75</sub> Se <sub>0.75</sub> Te <sub>0.25</sub>	2.552	2.972
		Mg <sub>0.25</sub> Zn <sub>0.75</sub> Se	2.606 1.91 <sup>a3@</sup> , 2.68 <sup>a3#</sup> , 2.94 <sup>a3\$</sup> , 1.427 <sup>b3*</sup> , 2.060 <sup>b3#</sup>	3.061
0.50	0.0	Mg <sub>0.50</sub> Zn <sub>0.50</sub> Te	2.358 1.67 <sup>a3@</sup> , 2.21 <sup>a3#</sup> , 2.78 <sup>a3\$</sup> , 1.456 <sup>b3*</sup> , 2.039 <sup>b3#</sup>	2.921
		Mg <sub>0.50</sub> Zn <sub>0.50</sub> Se <sub>0.25</sub> Te <sub>0.75</sub>	2.432	3.028
		Mg <sub>0.50</sub> Zn <sub>0.50</sub> Se <sub>0.50</sub> Te <sub>0.50</sub>	2.499	3.117
		Mg <sub>0.50</sub> Zn <sub>0.50</sub> Se <sub>0.75</sub> Te <sub>0.25</sub>	2.577	3.197
		Mg <sub>0.50</sub> Zn <sub>0.50</sub> Se	2.646 2.23 <sup>a3@</sup> , 2.96 <sup>a3#</sup> , 3.06 <sup>a3\$</sup> , 1.710 <sup>b3*</sup> , 2.558 <sup>b3#</sup>	3.399
0.75	0.0	Mg <sub>0.75</sub> Zn <sub>0.25</sub> Te	2.708 2.20 <sup>a3@</sup> , 2.68 <sup>a3#</sup> , 3.12 <sup>a3\$</sup> , 1.687 <sup>b3*</sup> , 2.270 <sup>b3#</sup>	3.255
		Mg <sub>0.75</sub> Zn <sub>0.25</sub> Se <sub>0.25</sub> Te <sub>0.75</sub>	2.737	3.379
		Mg <sub>0.75</sub> Zn <sub>0.25</sub> Se <sub>0.50</sub> Te <sub>0.50</sub>	2.847	3.441
		Mg <sub>0.75</sub> Zn <sub>0.25</sub> Se <sub>0.75</sub> Te <sub>0.25</sub>	2.947	3.543
		Mg <sub>0.75</sub> Zn <sub>0.25</sub> Se	3.084 2.64 <sup>a3@</sup> , 3.25 <sup>a3#</sup> , 3.35 <sup>a3\$</sup> , 2.027 <sup>b3*</sup> , 2.857 <sup>b3#</sup>	3.616
1.0	0.0	MgTe	3.444 3.49 <sup>c</sup> , 3.67 <sup>d</sup> , 2.90 <sup>e</sup> 2.325 <sup>e1*</sup> , 3.667 <sup>e1#</sup> , 2.354 <sup>f1%</sup> , 2.470 <sup>g1</sup> , 2.293 <sup>b2*</sup> , 3.153 <sup>b2#</sup> , 2.53 <sup>a3@</sup> , 3.62 <sup>a3#</sup> , 3.85 <sup>a3\$</sup> , 2.293 <sup>b3*</sup> , 3.156 <sup>b3#</sup>	3.877
		MgSe <sub>0.25</sub> Te <sub>0.75</sub>	3.514 2.300 <sup>b2*</sup> , 3.199 <sup>b2#</sup>	3.943
		MgSe <sub>0.50</sub> Te <sub>0.50</sub>	3.626 2.334 <sup>b2*</sup> , 3.277 <sup>b2#</sup>	4.091
		MgSe <sub>0.75</sub> Te <sub>0.25</sub>	3.698 2.398 <sup>b2*</sup> , 3.386 <sup>b2#</sup>	4.117
		MgSe	3.768 4.0 <sup>f</sup> , 3.60 <sup>g</sup> 2.206 <sup>f1%</sup> , 2.854 <sup>g1</sup> , 4.21 <sup>d1</sup> , 2.494 <sup>b2*</sup> , 3.529 <sup>b2#</sup> , 2.77 <sup>a3@</sup> , 3.92 <sup>a3#</sup> , 4.15 <sup>a3\$</sup> , 2.517 <sup>b3*</sup> , 3.584 <sup>b3#</sup>	4.189

Experimental data: <sup>a</sup>Ref. [22], <sup>b</sup>Ref. [20], <sup>c</sup>Ref. [32], <sup>d</sup>Ref. [30], <sup>e</sup>Ref. [31], <sup>f</sup>Ref. [29], <sup>g</sup>Ref. [24]

Earlier theoretical data: <sup>a1%</sup>Ref. [52] ⇒ LDA, <sup>a1&</sup>Ref. [52] ⇒ GW, <sup>b1</sup>Ref. [72], <sup>c1</sup>Ref. [53], <sup>d1</sup>Ref. [78], <sup>e1\*</sup>Ref. [71] ⇒ PBE-GGA, <sup>e1#</sup>Ref. [70] ⇒ EV-GGA, <sup>f1%</sup>Ref. [63] ⇒ LDA, <sup>g1</sup>Ref. [76], <sup>a2\*</sup>Ref. [73] ⇒ PBE-GGA, <sup>a2#</sup>Ref. [73] ⇒ EV-GGA, <sup>b2\*</sup>Ref. [75] ⇒ PBE-GGA, <sup>b2#</sup>Ref. [75] ⇒ EV-GGA, <sup>a3@</sup>Ref. [80] ⇒ WC-GGA, <sup>a3#</sup>Ref. [80] ⇒ EV-GGA, <sup>a3\$</sup>Ref. [80] ⇒ mBJ, <sup>b3\*</sup>Ref. [79] ⇒ PBE-GGA, <sup>b3#</sup>Ref. [79] ⇒ EV-GGA

theoretical band gap data are available in literature for comparison.

### 3.2.3 Concentration dependence of band gap

In this sub-section, we are going to present the results obtained from investigation of cationic ( $x$ ) and anionic ( $y$ ) concentration [ $x/y=0.0, 0.25, 0.50, 0.75$  and  $1.0$ ] dependence of fundamental energy band gap ( $E_g$ ) of the specimens within the  $\text{Mg}_x\text{Zn}_{1-x}\text{Se}_y\text{Te}_{1-y}$  quaternary system in two ways. Keeping the cationic (Mg) concentration  $x$  fixed at each of the five specified values, the calculated  $E_g$  is observed to be increased with increase in anionic (Se) concentration ( $y$ ) and each of such variations is presented in Fig. 4a, b, for mBJ and EV-GGA functional, respectively. Again, keeping the anionic (Se) concentration ( $y$ ) fixed at each of the five specific values, it is observed that the calculated  $E_g$  increases again with increase in cationic (Mg) concentration ( $x$ ) and each of such variations with mBJ and EV-GGA functional is presented in Fig. 4c, d, respectively. The variation of  $E_g$  with Se-concentration ( $y$ ) at each of the Mg-concentrations ( $x$ ), shown in Fig. 4a, b, as well as with Mg-concentration  $x$  at each of the Se-concentrations  $y$ , shown in Fig. 4c, d, shows nonlinearity under both the XC functional employed.

For any real alloy system, the nonlinear concentration dependence of band gap ( $E_g$ ) can be expressed in the following way:

$$E_g(x) = \alpha_g + \beta_g x + \delta_g x^2 \quad (2)$$

Here  $E_g(x)$  is the concentration-dependent band gap and the nonlinear coefficient  $\delta_g$  is called band-gap bowing or optical bowing parameter. For any specific XC functional, the band-gap bowing  $\delta_g$  for each alloy system is calculated by fitting  $E_g$  versus  $x$  or  $y$  curves with Eq. 2.

Now, the  $E_g$  versus  $y$  curves at each of the Mg-concentrations ( $x$ ) as well as  $E_g$  versus  $x$  curves at each of the Se-concentrations ( $y$ ) show downward bowing under both the XC functional employed. In case of the  $E_g$  versus anionic/cationic concentration curves, the calculated bowing parameters  $\delta_g$  with both the employed XC functional are also presented in Table 5. It is clear from Table 5 that  $\delta_g$  gradually increases under both the XC functional employed as we proceed from  $\text{ZnSe}_y\text{Te}_{1-y}$  to  $\text{MgSe}_y\text{Te}_{1-y}$  by replacing consecutively Zn with Mg atom(s). On the other hand,  $\delta_g$  gradually decreases under both the XC functional employed as we proceed from  $\text{Mg}_x\text{Zn}_{1-x}\text{Te}$  to  $\text{Mg}_x\text{Zn}_{1-x}\text{Se}$  by replacing successively Te with Se atom(s). A fair agreement is observed between our computed  $\delta_g$  and the reported experimental data for  $\text{Mg}_x\text{Zn}_{1-x}\text{Te}$  [30], but our computed  $\delta_g$  with mBJ functional is overestimated by 0.094 eV. In case of  $\text{Mg}_x\text{Zn}_{1-x}\text{Se}$  system, an excellent agreement is observed between our computed  $\delta_g$  and a couple of the reported experimental  $\delta_g$

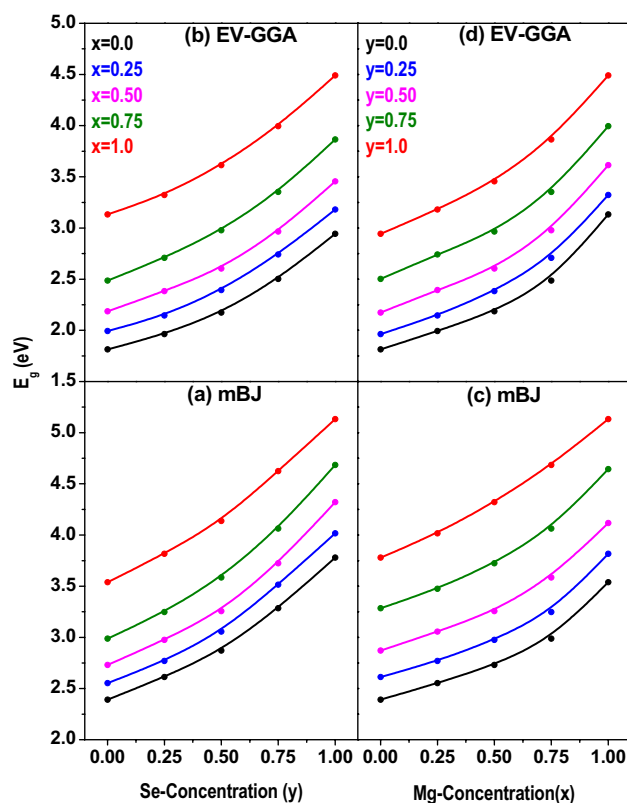


**Fig. 4** Variations of calculated **a** mBJ-induced minimum band gap  $E_g$  with Se-concentration  $y$  at each of the fixed Mg-concentrations  $x$ , **b** EV-GGA induced minimum band gap  $E_g$  with Se-concentration  $y$  at each of the fixed Mg-concentrations  $x$ , **c** mBJ-induced minimum band gap  $E_g$  with Mg-concentration  $x$  at each of the fixed Se-concentrations  $y$ , **d** EV-GGA induced minimum band gap  $E_g$  with Mg-concentration  $x$  at each of the fixed Se-concentrations  $y$  of the specimens within  $\text{Mg}_x\text{Zn}_{1-x}\text{Se}_y\text{Te}_{1-y}$  quaternary system

data [29, 32]. Moreover, in case of each of the  $\text{Mg}_x\text{Zn}_{1-x}\text{Se}$  and  $\text{Mg}_x\text{Zn}_{1-x}\text{Te}$  systems, our computed  $\delta_g$  with EV-GGA functional is underestimated by 0.164 eV and overestimated only by 0.064 eV, respectively, compared to the corresponding earlier theoretical data with same XC functional [79]. In case of other systems, any experimental or earlier theoretical  $\delta_g$  data are unavailable for comparison.

The Contour map of the calculated fundamental band gap versus the compositions  $x$  and  $y$  for  $\text{Mg}_x\text{Zn}_{1-x}\text{Se}_y\text{Te}_{1-y}$  quaternary system are presented in Fig. 5a, b for mBJ and EV-GGA functional, respectively. If  $E_g$  of four constituent binary compounds are known, the same of ternary or quaternary specimen, formed with them at any  $x$  and  $y$  in the range  $0 \leq x, y \leq 1$ , can be evaluated from such contour plots.

### 3.2.4 Density of States (DOS)

Using the density of states (DOS) of any semiconductor specimen, one can identify the atomic and orbital signature of various electronic states present in its band structure. In

**Table 5** Calculated optical bowing parameters ( $\delta_g$ ) from concentration dependence curves of  $E_g$

Alloy system	Fixed concentration	Variable concentration	$\delta_g$ (eV)	
			mBJ	EV-GGA
ZnSe <sub>y</sub> Te <sub>1-y</sub>	<i>x</i>	<i>y</i>	0.717	0.784
Mg <sub>0.25</sub> Zn <sub>0.75</sub> Se <sub>y</sub> Te <sub>1-y</sub>	<i>x</i>	<i>y</i>	0.801	0.821
Mg <sub>0.50</sub> Zn <sub>0.50</sub> Se <sub>y</sub> Te <sub>1-y</sub>	<i>x</i>	<i>y</i>	0.846	0.877
Mg <sub>0.75</sub> Zn <sub>0.25</sub> Se <sub>y</sub> Te <sub>1-y</sub>	<i>x</i>	<i>y</i>	0.903	0.964
MgSe <sub>y</sub> Te <sub>1-y</sub>	<i>x</i>	<i>y</i>	0.949	1.019
Mg <sub>x</sub> Zn <sub>1-x</sub> Te	<i>y</i>	<i>x</i>	0.764	1.524
			0.67 <sup>a</sup>	1.46 <sup>d</sup>
Mg <sub>x</sub> Zn <sub>1-x</sub> Se <sub>0.25</sub> Te <sub>0.75</sub>	<i>y</i>	<i>x</i>	0.714	1.337
Mg <sub>x</sub> Zn <sub>1-x</sub> Se <sub>0.50</sub> Te <sub>0.50</sub>	<i>y</i>	<i>x</i>	0.638	1.208
Mg <sub>x</sub> Zn <sub>1-x</sub> Se <sub>0.75</sub> Te <sub>0.25</sub>	<i>y</i>	<i>x</i>	0.524	1.084
Mg <sub>x</sub> Zn <sub>1-x</sub> Se	<i>y</i>	<i>x</i>	0.415	0.816
			0.40 <sup>b</sup>	0.98 <sup>d</sup>
			0.47 <sup>c</sup>	

<sup>a</sup>Ref. [30]=experimental data, <sup>b</sup>Ref. [29]=experimental data, <sup>c</sup>Ref. [32]=experimental data, <sup>d</sup>Ref. [79]=calculated data with EV-GGA

the present study, though we have computed the total density of states (TDOS) and partial density of states (PDOS) of each of the specimens within Mg<sub>x</sub>Zn<sub>1-x</sub>Se<sub>y</sub>Te<sub>1-y</sub> quaternary system, only TDOS (filled gray curves) and PDOS (colored lines) of the ternary and quaternary specimens within Mg<sub>0.25</sub>Zn<sub>0.75</sub>Se<sub>y</sub>Te<sub>1-y</sub> system for the whole anionic (Se) concentrations *y* and those within Mg<sub>x</sub>Zn<sub>1-x</sub>Se<sub>0.25</sub>Te<sub>0.75</sub> system for the whole range of cationic (Mg) concentrations *x* are presented as representatives in sets of Figs. 6a–e, 7a–e, respectively. In both the set of figures, the contributions of different atomic orbitals of the constituents of each of the concerned specimens within both the systems in their various regions of valence and conduction bands are clearly presented. Moreover, the effects of gradual anionic (*y*) substitution at fixed cationic (*x*) concentration on DOS from Fig. 6a–e as well as effects of successive cationic (*x*) substitution at fixed anionic (*y*) concentration on DOS from Fig. 7a–e can be clearly observed.

From Figs. 6a, 7a, we have observed from the TDOS and PDOS of ternary specimen Mg<sub>0.25</sub>Zn<sub>0.75</sub>Te and ZnSe<sub>0.25</sub>Te<sub>0.75</sub>, respectively, that different regions of valence and conduction band of the former are dominated by various orbitals of Mg, Zn and Te atoms, while the same for the later are dominated by various orbitals of Zn, Se and Te atoms. After initiation of doping of Se atom in the former as well as Mg atom in the latter and afterward, it is observed from Figs. 6b–d, 7b–d that in different regions of valence and conduction band of successive quaternary specimens, the contribution of different orbitals of chalcogen now comes from combined contribution of selenium and tellurium atoms in the former set, while the contribution of different orbitals of

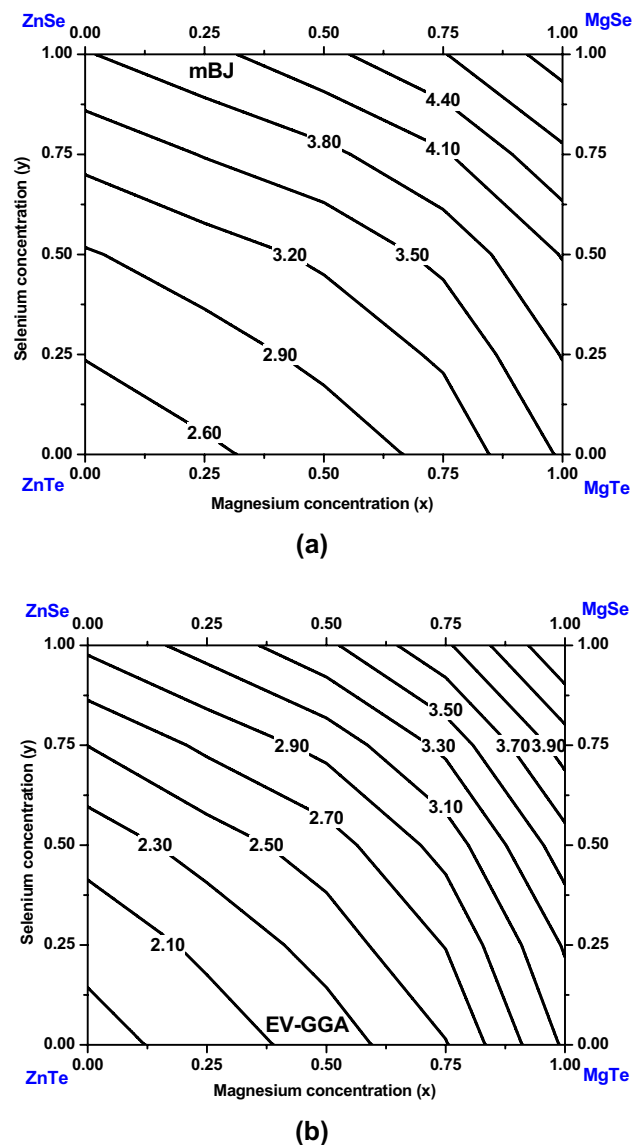


**Fig. 5** Contour map of the calculated minimum band gap  $E_g$  versus the compositions *x* and *y* for Mg<sub>x</sub>Zn<sub>1-x</sub>Se<sub>y</sub>Te<sub>1-y</sub> quaternary alloys with **a** mBJ, **b** EV-GGA functional

atom(s), other than chalcogens, now comes from combined contribution of Mg and Zn atoms in the latter set. Moreover, in different valence and conduction band regions of the said specimens, contribution from different orbitals of Se atom(s) gradually increases and those of Te gradually decrease with increase in Se-concentration in the former set, while contribution from different orbitals of Mg atom(s) gradually increases and those of Zn gradually decrease with increase in Mg-concentration in the later set. Finally, we have observed the complete domination of different orbitals of Se atoms in the TDOS and PDOS of ternary specimen Mg<sub>0.25</sub>Zn<sub>0.75</sub>Se in Fig. 6e, while those of Mg atoms in the TDOS and PDOS of ternary specimen MgSe<sub>0.25</sub>Te<sub>0.75</sub> in Fig. 7e. It should be

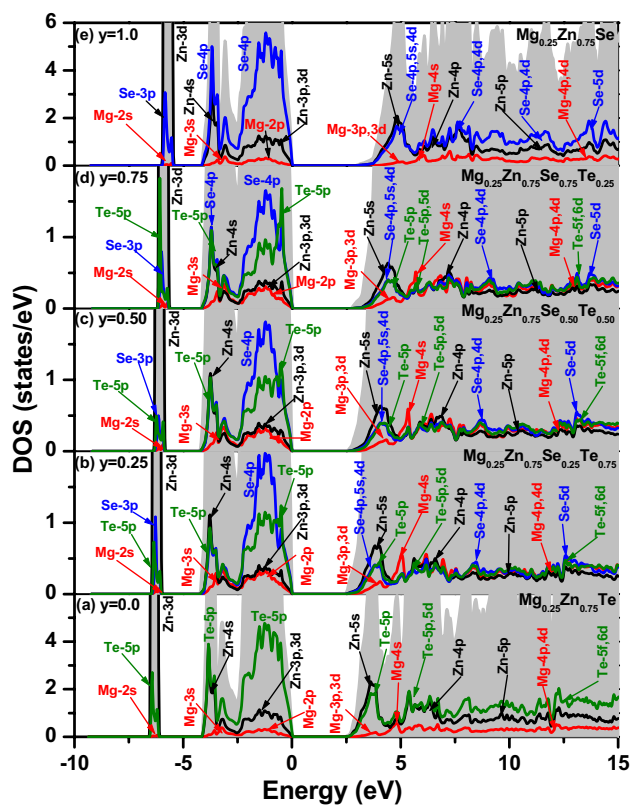


**Fig. 6** TDOS (filled gray curves) and PDOS (colored lines) of the specimens within  $\text{Mg}_{0.25}\text{Zn}_{0.75}\text{Se}_y\text{Te}_{1-y}$  quaternary alloys for **a**  $y=0.0$ , **b**  $y=0.25$ , **c**  $y=0.50$ , **d**  $y=0.75$ , **e**  $y=1.0$

noted that in different valence and conduction band regions of the said specimens, contributions of atomic orbitals of Mg and Zn in the former set and contributions of atomic orbitals of Se and Te in the later set remain unchanged due to their presence with fixed concentrations in the respective set.

In case of both the categories, the most interesting parts of DOS for each of the specimens are the regions of valence and conduction band closest to Fermi level, because most of the significant dipole-allowed optical transitions take place between different orbitals in these regions. We have observed in PDOS all the concerned specimens within  $\text{Mg}_{0.25}\text{Zn}_{0.75}\text{Se}_y\text{Te}_{1-y}$  system in Fig. 6a–e or PDOS all the concerned specimens within  $\text{Mg}_x\text{Zn}_{1-x}\text{Se}_{0.25}\text{Te}_{0.75}$  system in Fig. 7a–e that the contributions to valence band closest to Fermi level mostly comes from chalcogen-p states, i.e. either from Te-5p or from Se-4p or from both of them, while those from Zn-3p, 3d and Mg-2p are very low. On the other hand, the conduction band of these compounds near Fermi level are dominated almost equally by either Zn-5s or Mg-4s or both of them as well as by either Te-5p or collectively by Se-4p, 5s, 4d or by both the sets, while contribution from Mg-3p, 3d as well as Te- 6s, 5d are very low.

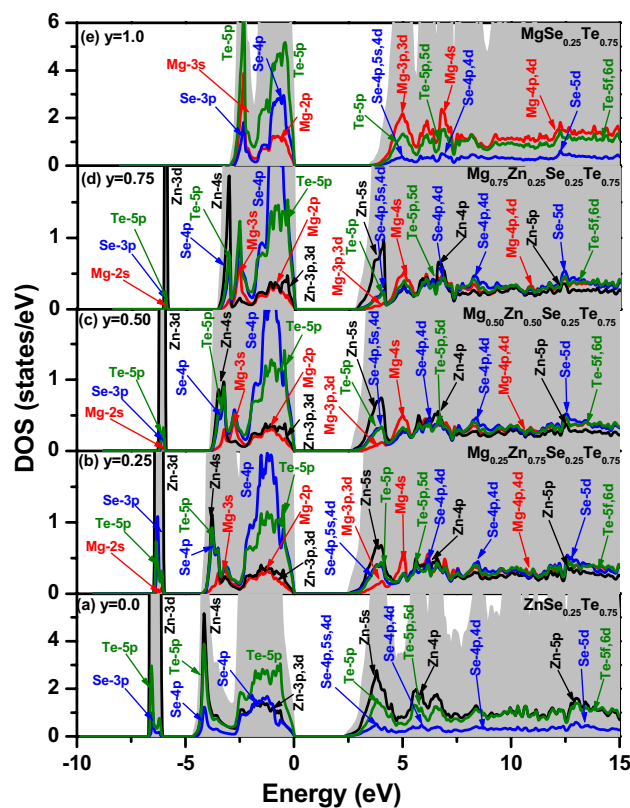


**Fig. 7** TDOS (filled gray curves) and PDOS (colored lines) of the specimens within  $\text{Mg}_x\text{Zn}_{1-x}\text{Se}_{0.25}\text{Te}_{0.75}$  quaternary alloys for **a**  $x=0.0$ , **b**  $x=0.25$ , **c**  $x=0.50$ , **d**  $x=0.75$ , **e**  $x=1.0$

### 3.3 Optical properties

When electromagnetic wave is incident on a crystal, electronic excitations take place within it and hence different optical features of that crystal can be observed and for any solid, such features are strongly dependent on the electronic properties of the said solid. Study of optical properties of a crystal gives us clear idea about the nature of its reaction to the frequency of the incident electromagnetic radiation and a material is selected for manufacturing optoelectronic devices on the basis of its optical features. Optical features of a material are studied mainly by its frequency dependent complex dielectric function  $\epsilon(\omega)$ , expressed as [101];

$$\epsilon(\omega) = \epsilon_1(\omega) + i\epsilon_2(\omega) \quad (3)$$

Here,  $\epsilon_1(\omega)$  and  $\epsilon_2(\omega)$  are the real and imaginary part of  $\epsilon(\omega)$ , respectively. The refractive index  $n(\omega)$ , extinction coefficient  $k(\omega)$ , normal incidence reflectivity  $R(\omega)$ , optical conductivity  $\sigma(\omega)$ , optical absorption coefficient  $\alpha(\omega)$  and energy loss function  $L(\omega)$  of any semiconductor specimen can be derived from its  $\epsilon_1(\omega)$  and  $\epsilon_2(\omega)$  and their expressions and some of their ancillary parameters, employed in the

present study, are presented as Eqs. SQ1–SQ14 in Section-I of the Supplementary Materials.

### 3.3.1 Frequency response curves of different optical parameters

In the present work, we have calculated the frequency responses of the  $\epsilon_1(\omega)$ ,  $\epsilon_2(\omega)$ ,  $n(\omega)$ ,  $k(\omega)$ ,  $R(\omega)$ ,  $\sigma(\omega)$ ,  $\alpha(\omega)$  and  $L(\omega)$  of the binary, ternary and quaternary specimens within  $\text{Mg}_x\text{Zn}_{1-x}\text{Se}_y\text{Te}_{1-y}$  system up to incident energy 30.0 eV employing mBJ and EV-GGA functional using Eqs. SQ1–SQ14. The frequency responses of  $\epsilon_1(\omega)$  and  $\epsilon_2(\omega)$  with mBJ functional are presented in Figs. 8 and 9, respectively, in the main text, while those of  $n(\omega)$ ,  $k(\omega)$ ,  $R(\omega)$ ,  $\sigma(\omega)$ ,  $\alpha(\omega)$  and  $L(\omega)$  with same XC functional are presented in Figs. S7–S12 in the Supplementary materials. In each of these Figures, we have presented the frequency response curves of specimens in the five left panels, where each of the five curves in any panel are formed with a fixed cationic (Mg) concentration ( $x$ ), but with five different anionic (Se) concentrations ( $y$ ). On the other hand, the curves formed with a fixed anionic (Se) concentration ( $y$ ), but with all the five different cationic (Mg) concentrations ( $x$ ) are presented in each of the five right panels.

In each of the  $\epsilon_1(\omega)$  spectra in Fig. 8, we have observed that  $\epsilon_1(\omega)$  is substantially high with prominent peak(s) up to about 6.0 eV. Again, in the mid-energy region about 6.5–15.0 eV, the calculated  $\epsilon_1(\omega)$  in all the spectra become negative and in the subsequent energy region beyond 15.0 eV,  $\epsilon_1(\omega)$  in all the spectra again achieve very low positive value. The negative value of  $\epsilon_1(\omega)$  is a signature of metallic behavior of any of these specimens as a result of reflection of incident electromagnetic radiation by it in this spectral range. From each of the  $n(\omega)$  spectra in Fig. S7, it is observed that  $n(\omega)$  is significantly high up and show prominent peaks up to about 6.5 eV of incident energy, while we have observed  $n(\omega) < 1$  in the subsequent higher energy region for each specimen. On the other hand, we have observed in the  $R(\omega)$  spectra of all the specimens in Fig. S8 that  $R(\omega)$  is significantly high in the broad energy region 3.5–15.5 eV and then gradually drops down to very low value in the subsequent energy region.

In the  $\epsilon_2(\omega)$  spectra of all the specimens within  $\text{Mg}_x\text{Zn}_{1-x}\text{Se}_y\text{Te}_{1-y}$  quaternary system in Fig. 9, it is observed that  $\epsilon_2(\omega)$  is significantly high in the incident energy region 4.0–10.0 eV, while it becomes insignificant in the subsequent energy region in case of each specimen. The HOMO–LUMO electronic transitions between different atomic orbital of valence and conduction band are responsible for occurrence of peak(s) in the  $\epsilon_2(\omega)$  spectra of each specimen in the aforesaid energy region.

The most intense peaks in the  $\epsilon_2(\omega)$  spectra of ZnSe and ZnTe at 6.14 eV and 4.99 eV, respectively, are due to strong

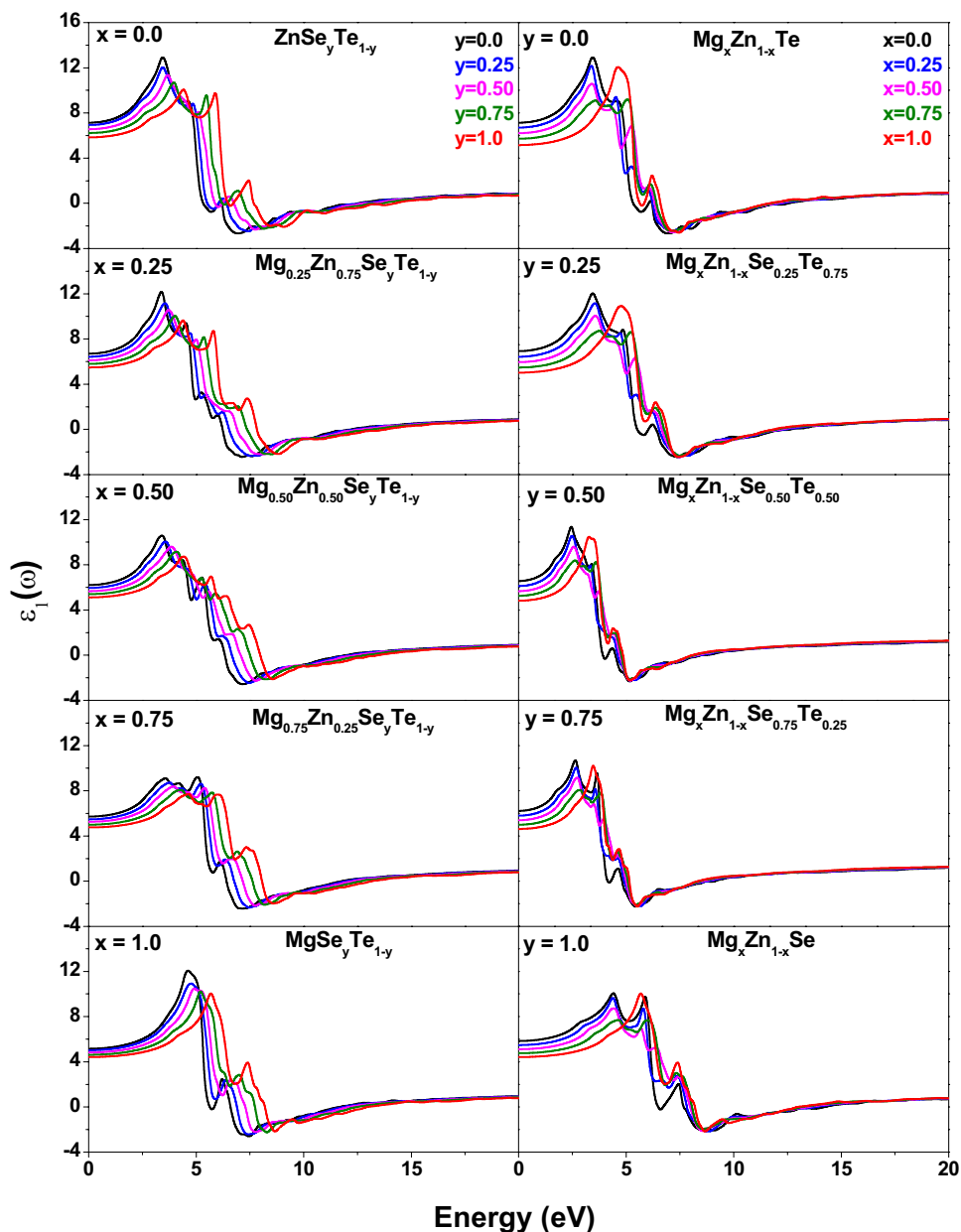
electronic transitions Se-4p  $\rightarrow$  Zn-5s and Te-5p  $\rightarrow$  Zn-5s, respectively, while comparatively much weakly intense peaks at the 7.58 eV and 6.24 eV in the  $\epsilon_2(\omega)$  spectra of ZnSe and ZnTe, respectively, are due to comparatively much weak electronic transitions Se-4p  $\rightarrow$  Zn-4p and Te-5p  $\rightarrow$  Zn-4p, respectively, from occupied valence to unoccupied conduction band. On the other hand, the most intense peaks in the  $\epsilon_2(\omega)$  spectra of MgSe and MgTe at 6.38 eV and 5.32 eV, respectively, are due to strong electronic transitions Se-4p  $\rightarrow$  Mg-4s and Te-5p  $\rightarrow$  Mg-4s, respectively, while slightly weaker peaks at 7.61 eV and 6.54 eV in the  $\epsilon_2(\omega)$  spectra of MgSe and MgTe are due to comparatively weak electronic transitions Se-4p  $\rightarrow$  Mg-4p and Te-5p  $\rightarrow$  Mg-4p, respectively, from occupied valence to unoccupied conduction band. It should be noted that the intensity difference between two peaks in the  $\epsilon_2(\omega)$  spectra of each of the ZnSe and ZnTe are much higher compared to that between the two peaks occurred in the  $\epsilon_2(\omega)$  spectra of each of the MgSe and MgTe.

In case of  $\epsilon_2(\omega)$  spectra of anionic ternary specimen  $\text{ZnSe}_{0.25}\text{Te}_{0.75}$ , the first intense peak at 5.24 eV is due to combined effort of a very strong Te-5p  $\rightarrow$  Zn-5s and much weaker Se-4p  $\rightarrow$  Zn-5s electronic transitions, while that arising out in the  $\epsilon_2(\omega)$  spectra of  $\text{MgSe}_{0.25}\text{Te}_{0.75}$  at 5.54 eV is due to combined effort of a very strong Te-5p  $\rightarrow$  Mg-4s and much weaker Se-4p  $\rightarrow$  Mg-4s electronic transitions from valence band to conduction band. On the other hand, the next intense peak at 6.49 eV in the  $\epsilon_2(\omega)$  spectra of  $\text{ZnSe}_{0.25}\text{Te}_{0.75}$  is due to combined effort of strong Te-5p  $\rightarrow$  Zn-4p and much weaker Se-4p  $\rightarrow$  Zn-4p transitions, while that at 6.87 eV in the  $\epsilon_2(\omega)$  spectra of  $\text{MgSe}_{0.25}\text{Te}_{0.75}$  is due to combined effort of strong Te-5p  $\rightarrow$  Mg-4p and much weaker Se-4p  $\rightarrow$  Mg-4p electronic transitions from valence band to conduction band. It is also observed that intensity difference between two peaks in the  $\epsilon_2(\omega)$  spectra of  $\text{ZnSe}_{0.25}\text{Te}_{0.75}$  is higher compared to that between the two peaks occurred in the  $\epsilon_2(\omega)$  spectra of each of  $\text{MgSe}_{0.25}\text{Te}_{0.75}$ . It is also to be noted that intensity of transitions originating from Se-4p and gradually dominating over the transitions originating from Se-4p and peak positions clearly exhibits marginal blue shift in both the  $\text{ZnSe}_y\text{Te}_{1-y}$  and  $\text{MgSe}_y\text{Te}_{1-y}$  systems with increase in Se-concentration ( $y$ ).

In case of  $\epsilon_2(\omega)$  spectra of cationic ternary specimen  $\text{Mg}_{0.25}\text{Zn}_{0.75}\text{Se}$  and  $\text{Mg}_{0.25}\text{Zn}_{0.75}\text{Te}$ , the first intense peak arising at 6.00 eV and 4.77 eV, respectively, are due to combined effort of electronic transitions Se-4p  $\rightarrow$  Zn-5s, Se-4p  $\rightarrow$  Mg-4s and Te-5p  $\rightarrow$  Zn-5s, Te-5p  $\rightarrow$  Mg-4s, respectively, from valence to conduction band. On the other hand, the next intense peaks, arising at 7.74 eV and 5.54 eV, respectively, are due to electronic transitions Se-4p  $\rightarrow$  Zn-4p, Se-4p  $\rightarrow$  Mg-4p and Te-5p  $\rightarrow$  Zn-4p, Te-5p  $\rightarrow$  Mg-4p, respectively, from valence to conduction band. Also, we have observed substantial intensity difference between two



**Fig. 8** Frequency response curves of  $\varepsilon_1(\omega)$  for the specimens within  $\text{Mg}_x\text{Zn}_{1-x}\text{Se}_y\text{Te}_{1-y}$  quaternary system for different Se-concentrations at each of the Mg-concentrations (5 left panels) and for different Mg-concentrations at each of the Se-concentrations (5 right panels)

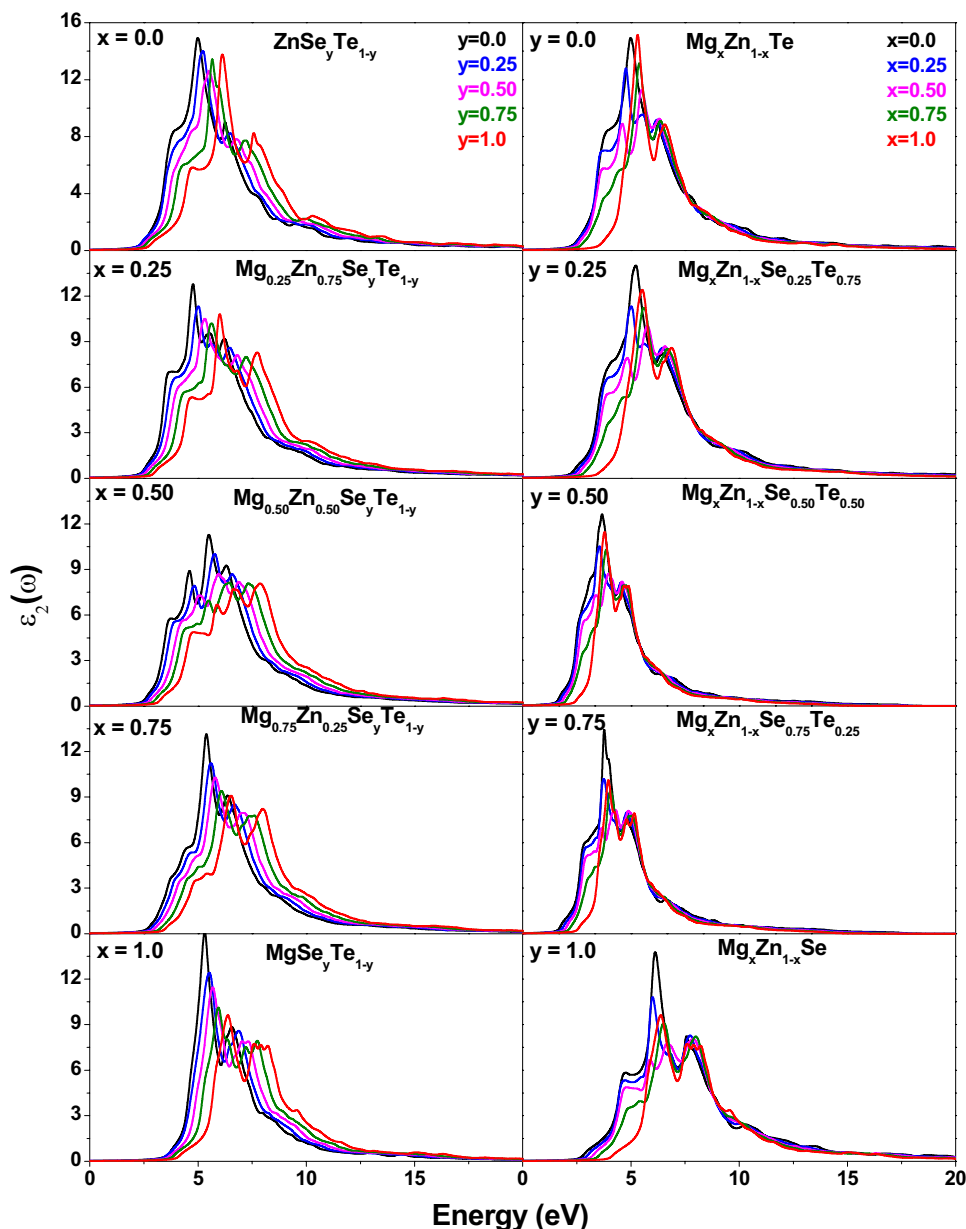


peaks in the  $\varepsilon_2(\omega)$  spectra of each of the said cationic ternary alloys. It is to be noted that intensity of transitions terminates to Mg-4s, 4p gradually dominating over the transitions to Zn-5s, 4p with increase in Mg-concentration ( $x$ ) in both the  $\text{Mg}_x\text{Zn}_{1-x}\text{Se}$  and  $\text{Mg}_x\text{Zn}_{1-x}\text{Te}$  systems.

In case of  $\varepsilon_2(\omega)$  spectra of nine quaternary specimens  $\text{Mg}_{0.25}\text{Zn}_{0.75}\text{Se}_y\text{Te}_{1-y}$ ,  $\text{Mg}_{0.50}\text{Zn}_{0.50}\text{Se}_y\text{Te}_{1-y}$  and  $\text{Mg}_{0.75}\text{Zn}_{0.25}\text{Se}_y\text{Te}_{1-y}$  at  $y = 0.25, 0.50$  &  $0.75$ , the first intense peak in each spectra is due to combined effort of  $\text{Te-5p} \rightarrow \text{Zn-5s}$ ,  $\text{Te-5p} \rightarrow \text{Mg-4s}$ ,  $\text{Se-4p} \rightarrow \text{Zn-5s}$  and  $\text{Se-4p} \rightarrow \text{Mg-4s}$  electronic transitions from valence band to conduction band. On the other hand, the comparatively low intense peak in each spectrum in the higher energy side of the first peak is due to  $\text{Te-5p} \rightarrow \text{Zn-4p}$ ,

$\text{Te-5p} \rightarrow \text{Mg-4p}$ ,  $\text{Se-4p} \rightarrow \text{Zn-4p}$  and  $\text{Se-4p} \rightarrow \text{Mg-4p}$  electronic transitions from valence band to conduction band. Keeping Mg-concentration ( $x$ ) fixed, if we gradually increase the Se-concentration ( $y$ ) to 0.50 and then to 0.75, the transitions originating from Se-4p become gradually stronger compared to the transitions originating from Te-5p in both the peaks of the  $\varepsilon_2(\omega)$  spectra of each of the corresponding quaternary specimens. On the other hand, if we gradually increase the Mg-concentration ( $x$ ) to 0.50 and then to 0.75 keeping Se-concentration ( $y$ ) fixed, the transitions terminating to Mg-4s, 4p become gradually stronger compared to the transitions terminating to Zn-5s, 4p in both the peaks of the  $\varepsilon_2(\omega)$  spectra of each of the corresponding quaternary specimens.

**Fig. 9** Frequency response curves of  $\epsilon_2(\omega)$  for the specimens within  $\text{Mg}_x\text{Zn}_{1-x}\text{Se}_y\text{Te}_{1-y}$  quaternary system for different Se-concentrations at each of the Mg-concentrations (5 left panels) and for different Mg-concentrations at each of the Se-concentrations (5 right panels)



In the frequency response spectra of  $k(\omega)$  in Fig. S9, we have observed  $k(\omega) > 1$  throughout the incident energy region 5.0–15.0 eV. Also we have observed peaks having maximum amplitude  $k(\omega) > 2$  in the  $k(\omega)$  spectra of each of the specimens. Therefore, incident photons with energy in this specific range suffer more difficulty during their penetration through each of these specimens compared the photons having energy beyond this energy region in the  $k(\omega)$  spectra [100].

The  $\sigma(\omega)$  spectra of each specimen in Fig. S10 show a couple of peaks in the narrow incident energy region 4.0–10.0 eV with peak values  $\sigma(\omega)$  greater than at least  $7000 \text{ } \Omega^{-1} \text{ cm}^{-1}$ , while  $\sigma(\omega)$  becomes very low beyond this energy region. The  $\alpha(\omega)$  spectra of each specimen in Figures S11

show substantial optical absorption [ $\alpha(\omega) > 100$ ] in the wide 5.0–15.0 eV incident energy region and maxima, having  $\alpha(\omega)$  more than 175, occurs in this narrow energy segment.

Electron energy loss function  $L(\omega)$  is used to investigate inelastically scattered electrons by atoms in a lattice site and to calculate the amount of energy loss during such scattering process. It is obvious from Eq. SQ14 that  $L(\omega)$  of any specimen is strongly dependent on its  $\epsilon_2(\omega)$  [102] and their frequency responses are qualitatively opposite in nature. In the  $L(\omega)$  spectra of each specimen in Fig. S12, we have observed that  $L(\omega)$  is insignificant because of the significantly high value of  $\epsilon_2(\omega)$  in the energy region up to 11.0 eV. It indicates that inelastic scattering of only few electrons occurs and hence minimum energy loss occurs due to it in this energy

region. On the other hand,  $L(\omega)$  gradually increases beyond 11.0 eV of incident energy because of the insignificant value of  $\varepsilon_2(\omega)$  in this energy region. As a result, number of inelastically scattered electrons and hence energy loss due to it gradually increases. It is also observed that  $L(\omega)$  for each specimen is significantly high with peak(s) in the incident energy region 12.0–20.0 eV, because  $\varepsilon_2(\omega)$  is significantly low in this region. It should be noted that we can measure the plasma resonance frequency for any specimen from the energetic position of the most intense peak present in the  $L(\omega)$  spectra of that specimen.

### 3.3.2 Zero-frequency limits and critical points in different optical spectra

In the present study, we have calculated zero-frequency limits  $\varepsilon_1(0)$ ,  $n(0)$  and  $R(0)$  of the  $\varepsilon_1(\omega)$ ,  $n(\omega)$  and  $R(\omega)$  spectra, respectively, for the binary, ternary and quaternary specimens within the  $\text{Mg}_x\text{Zn}_{1-x}\text{Se}_y\text{Te}_{1-y}$  quaternary system. They are the value of the optical parameter  $\varepsilon_1(\omega)$ ,  $n(\omega)$  and  $R(\omega)$  in their respective spectra at zero-incident energy/frequency and known as static dielectric constant, static refractive index and static reflectivity, respectively. Our calculated static dielectric constants  $\varepsilon_1(0)$ , static refractive index  $n(0)$  and static reflectivity  $R(0)$  of all the specimens under  $\text{Mg}_x\text{Zn}_{1-x}\text{Se}_y\text{Te}_{1-y}$  quaternary system with both the EV-GGA and mBJ functional are presented in Table 6 along with available experimental or earlier theoretical data of few specimens for comparison.

Few available experimental  $\varepsilon_1(0)$  data for ZnSe and ZnTe [25, 26] are incorporated in Table 6 for comparison, while no experimental  $\varepsilon_1(0)$  data for zinc-blende MgSe and MgTe are available. We have also compared our computed  $\varepsilon_1(0)$  for the binary compounds with some earlier theoretical data for ZnSe [61, 82] and ZnTe [61, 81, 82] as well as MgSe [65, 77, 83] and MgTe [65, 80, 81, 83]. Our mBJ-based computed  $\varepsilon_1(0)$  data for ZnSe and ZnTe are in excellent agreement with the corresponding experimental data. Also, they are closer to corresponding respective experimental data compared to most of the respective earlier theoretical findings due to excellent matching of our mBJ-based computed band gaps with respective experimental findings. On the other hand, our EV-GGA based  $\varepsilon_1(0)$  for ZnSe and ZnTe are fairly overestimated with respect to the corresponding experimental data due to fair underestimation of our EV-GGA based computed band gaps with respect to corresponding experimental data.

In case of MgSe and MgTe, our computed data  $\varepsilon_1(0)$  with the mBJ functional is underestimated with respect to some of the corresponding earlier theoretical data [80, 83] due to our mBJ based improved band gaps, while fair agreement is observed between our EV-GGA based calculated  $\varepsilon_1(0)$  and

the corresponding earlier theoretical data for MgTe [80, 83]. In case of any of the ternary or quaternary specimens, no experimental or earlier theoretical  $\varepsilon_1(0)$  data is available in literature to compare. It is also observed from Table 6 that our computed  $\varepsilon_1(0)$  for each specimen with both the functionals shows the trend  $\varepsilon_1(0)^{\text{EV-GGA}} > \varepsilon_1(0)^{\text{mBJ}}$  because of the fact that our calculated band gap follows the trend  $E_g^{\text{mBJ}} > E_g^{\text{EV-GGA}}$ . All the aforesaid dependence of  $\varepsilon_1(0)$  on band-gap ( $E_g$ ) can be explained by the approximate relation between the  $E_g$  and  $\varepsilon_1(0)$ , as proposed by Penn [103]:

$$\varepsilon_1(0) \approx 1 + \left( \frac{\hbar\omega_p}{E_g} \right)^2 \quad (4)$$

Equation 4 indicates that  $\varepsilon_1(0)$  is approximately inversely proportional to the square of  $E_g$  and hence  $\varepsilon_1(0)$  of any material increases with decrease in its band gap and vice versa.

For any specimen, the approximate relationship between  $n(0)$  and  $\varepsilon_1(0)$  is [101]

$$n(0) \approx \sqrt{\varepsilon_1(0)} \quad (5)$$

On the other hand, since the extinction coefficient  $k(\omega)=0$  at zero incident frequency, the relationship between  $n(0)$  and  $R(0)$ , using Eq. SQ10, becomes

$$R(0) = \left[ \frac{1 - n(0)}{1 + n(0)} \right]^2 \quad (6)$$

This ultimately gives us the relation between  $R(0)$  and  $\varepsilon_1(0)$  as follows;

$$R(0) = \left[ \frac{1 - \sqrt{\varepsilon_1(0)}}{1 + \sqrt{\varepsilon_1(0)}} \right]^2 \quad (7)$$

Any experimental  $n(0)$  and  $R(0)$  data for binary, ternary and quaternary specimens is unavailable for comparison. On the other hand, some earlier theoretical  $n(0)$  and  $R(0)$  data for ZnSe and ZnTe [80–82] as well as MgSe and MgTe [77, 80, 83] are available in literature. In case anionic ternary alloys  $\text{ZnSe}_y\text{Te}_{1-y}$  and  $\text{MgSe}_y\text{Te}_{1-y}$  as well as any of the quaternary specimens, no earlier theoretical  $n(0)$  and  $R(0)$  data are available, while some earlier theoretical data  $n(0)$  and  $R(0)$  is available in literature for cationic ternary alloys  $\text{Mg}_x\text{Zn}_{1-x}\text{Se}$  [65, 80] and  $\text{Mg}_x\text{Zn}_{1-x}\text{Te}$  [80, 81]. It is to be noted that  $n(0)$  and  $R(0)$  has been calculated with mBJ functional in one of the earlier theoretical studies [80]. Our mBJ based computed  $n(0)$  and  $R(0)$  for each of these binary and cationic ternary specimens agrees well but marginally underestimated with respect to the corresponding earlier mBJ based data [80] as well as others [65, 77, 81–83]. This is due to our comparatively higher mBJ based band gap of each of these specimens relative to the

**Table 6** Calculated  $\epsilon_1(0)$ ,  $n(0)$  and  $R(0)$  of binary, ternary and quaternary specimens within  $Mg_xZn_{1-x}Se_yTe_{1-y}$  alloys using mBJ and EV-GGA functional

x	y	Specimen	Zero-frequency limit					
			$\epsilon_1(0)$		$n(0)$		$R(0)$	
			mBJ	EV-GGA	mBJ	EV-GGA	mBJ	EV-GGA
0.0	0.0	ZnTe	7.135	7.418	2.576	2.824	0.194	0.214
			7.28 <sup>a</sup>					
			7.99 <sup>a1</sup>		2.67 <sup>b1</sup>	2.58 <sup>c1</sup>	0.197 <sup>b1</sup>	
			7.13 <sup>b1</sup>		2.65 <sup>d1</sup>		0.2054 <sup>d1</sup>	
			6.67 <sup>c1</sup>					
	0.25	ZnSe <sub>0.25</sub> Te <sub>0.75</sub>	6.928	7.219	2.535	2.786	0.189	0.209
			6.562	6.839	2.462	2.715	0.178	0.199
			6.222	6.481	2.392	2.646	0.168	0.190
			5.742	6.202	2.271	2.593	0.157	0.182
			5.9 <sup>b</sup>					
0.25	0.0	Mg <sub>0.25</sub> Zn <sub>0.75</sub> Te	6.705	6.937	2.294	2.714	0.158	0.199
					2.48 <sup>c1</sup>		0.163 <sup>d1</sup>	
					2.35 <sup>d1</sup>			
			6.429	6.641	2.255	2.658	0.149	0.192
			6.116	6.342	2.219	2.598	0.142	0.183
	0.25	Mg <sub>0.25</sub> Zn <sub>0.75</sub> Se <sub>0.25</sub> Te <sub>0.75</sub>	6.116	6.342	2.219	2.598	0.142	0.183
			5.801	6.099	2.152	2.528	0.136	0.174
			5.476	5.651	2.117	2.456	0.131	0.163
					2.14 <sup>d1</sup>		0.133 <sup>c1</sup>	
0.50	0.0	Mg <sub>0.50</sub> Zn <sub>0.50</sub> Te	6.211	6.574	2.217	2.584	0.146	0.181
					2.22 <sup>c1</sup>		0.156 <sup>d1</sup>	
					2.30 <sup>d1</sup>			
			5.952	6.227	2.164	2.534	0.138	0.174
			5.667	5.949	2.133	2.476	0.132	0.166
	0.50	Mg <sub>0.50</sub> Zn <sub>0.50</sub> Se <sub>0.50</sub> Te <sub>0.50</sub>	5.667	5.949	2.133	2.476	0.132	0.166
			5.398	5.668	2.103	2.417	0.126	0.157
			5.113	5.359	2.078	2.369	0.121	0.147
					2.13 <sup>d1</sup>		0.1311 <sup>e1</sup>	
0.75	0.0	Mg <sub>0.75</sub> Zn <sub>0.25</sub> Te	5.717	5.921	2.171	2.449	0.135	0.162
					2.21 <sup>c1</sup>		0.1398 <sup>d1</sup>	
					2.19 <sup>d1</sup>			
			5.475	5.771	2.131	2.398	0.128	0.156
			5.255	5.584	2.071	2.355	0.118	0.149
	0.75	Mg <sub>0.75</sub> Zn <sub>0.25</sub> Se <sub>0.25</sub> Te <sub>0.75</sub>	5.255	5.584	2.071	2.355	0.118	0.149
			4.998	5.337	2.001	2.299	0.111	0.141
			4.756	5.082	1.952	2.244	0.105	0.132
					1.97 <sup>d1</sup>		0.107 <sup>e1</sup>	
1.0	0.0	MgTe	5.156	5.436	2.095	2.299	0.129	0.140
			4.46 <sup>c1</sup>		2.11 <sup>c1</sup>		0.1363 <sup>d1,f1</sup>	
			5.495 <sup>d1</sup>		2.17 <sup>d1,f1</sup>			
			6.091 <sup>e1</sup>					
			5.48 <sup>g1</sup>					
	0.25	MgSe <sub>0.25</sub> Te <sub>0.75</sub>	5.021	5.292	2.046	2.266	0.121	0.136
			4.822	5.106	1.991	2.222	0.113	0.129
			4.624	4.914	1.954	2.177	0.106	0.122
			4.416	4.725	1.911	2.135	0.097	0.119
			5.167 <sup>c1</sup>		1.95 <sup>d1</sup>		0.1049 <sup>d1</sup>	
1.0	MgSe	4.418 <sup>f1</sup>		2.10 <sup>g1</sup>				
		4.43 <sup>g1</sup>						

Experimental data: <sup>a</sup>Ref. [26], <sup>b</sup>Ref. [25]

Earlier theoretical data: <sup>a1</sup>Ref. [61], <sup>b1</sup>Ref. [82], <sup>c1</sup>Ref. [81], <sup>d1</sup>Ref. [80], <sup>e1</sup>Ref. [65], <sup>f1</sup>Ref. [77], <sup>g1</sup>Ref. [83]

respective earlier theoretical band gap data [80] with same XC functional. It is also observed from Table 6 that our computed  $n(0)$  and  $R(0)$  for each specimen with the couple of XC functional show the trend  $n(0)^{EV-GGA} > n(0)^{mBJ}$  as well as  $R(0)^{EV-GGA} > R(0)^{mBJ}$ , respectively, because of the fact that our calculated band gap follow the trend  $E_g^{mBJ} > E_g^{EV-GGA}$ . All the aforesaid dependence of  $n(0)$  on band-gap ( $E_g$ ) can be explained by the following relation between the  $E_g$  and  $n(0)$ , obtained by combining Eqs. 4 and 5, as;

$$n(0) \approx \sqrt{1 + \left(\frac{\hbar\omega_p}{E_g}\right)^2} \quad (8)$$

The dependence of  $R(0)$  on band-gap ( $E_g$ ) can also be explained by the following relation between the  $E_g$  and  $R(0)$ , obtained by combining Eqs. 7 and 8, as;

$$R(0) = \left[ \frac{1 - \sqrt{1 + \left(\frac{\hbar\omega_p}{E_g}\right)^2}}{1 + \sqrt{1 + \left(\frac{\hbar\omega_p}{E_g}\right)^2}} \right]^2 \quad (9)$$

Equation 8 states that  $n(0)$  and is approximately inversely proportional to  $E_g$  and hence an increase in band gap results in a decrease in static dielectric constant of a material and vice versa. Also, an increase in  $R(0)$  with decrease in band gap and vice versa is the outcome of Eq. 9.

The critical points in the  $\epsilon_2(\omega)$ ,  $k(\omega)$ ,  $\sigma(\omega)$  and  $\alpha(\omega)$  spectra is the threshold incident energy  $E_c$  (eV) at which each of these optical parameters starts responding to the incident radiation. It is to be noted that a semiconductor specimen with higher fundamental band gap requires higher critical point energy in its  $\epsilon_2(\omega)$  and  $k(\omega)$  spectra and vice versa according to the Kramers–Kronig transformations between  $\epsilon_1(\omega)$  and  $\epsilon_2(\omega)$  [Eqs. SQ3 and SQ4] as well as those between  $n(\omega)$  and  $k(\omega)$  [Eqs. SQ6 and SQ7], respectively. Since  $\sigma(\omega)$  is proportional to  $\epsilon_2(\omega)$  and  $\alpha(\omega)$  is proportional to  $k(\omega)$  according to the Eqs. SQ11 and SQ13, respectively, the similar band gap dependence of critical points are observed in the  $\sigma(\omega)$  and  $\alpha(\omega)$  spectra. The critical points in the aforesaid spectra of all the binary, ternary and quaternary specimens under  $Mg_xZn_{1-x}Se_yTe_{1-y}$  quaternary system with both the EV-GGA and mBJ functional are presented in Table 7, but no experimental critical point data for any of these specimens are available for comparison. On the other hand, in the earlier calculated critical points in the  $\epsilon_2(\omega)$  and  $\sigma(\omega)$  spectra, only the binary specimens MgSe and MgTe are available in a literature [77]. It is also observed from Table 7 that our mBJ based computed critical points in each of the  $\epsilon_2(\omega)$  spectra of MgSe and MgTe are higher than the

respective critical points, reported in an earlier theoretical study [77], because our calculated band gaps for MgSe and MgTe with mBJ functional are much higher than the respective band gaps, reported in that earlier theoretical study with EV-GGA functional. It is clear from Table 7 that our calculated critical point in each of the  $\epsilon_2(\omega)$ ,  $k(\omega)$ ,  $\sigma(\omega)$  and  $\alpha(\omega)$  spectra of any specimen maintains the trend  $E_c^{mBJ} > E_c^{EV-GGA}$  since our calculated band gaps with both the XC functional follow the trend  $E_g^{mBJ} > E_g^{EV-GGA}$ .

### 3.3.3 Concentration dependence of Zero-frequency limits and critical points

The zero-frequency limits  $\epsilon_1(0)$ ,  $n(0)$  and  $R(0)$  as well as critical points in the  $\epsilon_2(\omega)$ ,  $k(\omega)$ ,  $\sigma(\omega)$  and  $\alpha(\omega)$  spectra of the specimens within  $Mg_xZn_{1-x}Se_yTe_{1-y}$  quaternary system are strongly dependent on the cationic (Mg) and anionic (Se) concentrations  $x$  and  $y$ , respectively. We again investigated the concentration dependence of these optical constants in two ways.

Keeping the cationic (Mg) concentration ( $x$ ) fixed at each of the five specified values, each of the calculated zero-frequency limits  $\epsilon_1(0)$ ,  $n(0)$  and  $R(0)$  under both the employed XC functional decreases, while the critical points in each of the  $\epsilon_2(\omega)$ ,  $k(\omega)$ ,  $\sigma(\omega)$  and  $\alpha(\omega)$  spectra increases with increase in anionic (Se) concentration  $y$ , as observed from Tables 6 and 7, respectively. Also, at each of the five fixed anionic (Se) concentrations  $y$ , each of the calculated  $\epsilon_1(0)$ ,  $n(0)$  and  $R(0)$  under both the employed XC functional again decreases, while the critical points in each of the  $\epsilon_2(\omega)$ ,  $k(\omega)$ ,  $\sigma(\omega)$  and  $\alpha(\omega)$  spectra increase again with increase in cationic (Mg) concentration  $x$ , as presented in Tables 6 and 7, respectively. It is to be noted that in both types of variations, our calculated band gaps with each of the mBJ and EV-GGA functional increase. Therefore, both the trends of variation of each of the  $\epsilon_1(0)$ ,  $n(0)$  and  $R(0)$  as well as critical points in each of the said spectra with cationic ( $x$ ) and anionic ( $y$ ) concentrations are strongly related to the concentration ( $x/y$ ) dependence of band gaps and an increase in band gap results in a decrease in each of these zero-frequency limits and increase in critical points, respectively, and vice versa. Therefore, such band gap dependence of each of the  $\epsilon_1(0)$ ,  $n(0)$  and  $R(0)$  is again well supported by Eqs. 4, 8 and 9, respectively, while that of each of the critical points in the  $\epsilon_2(\omega)$ ,  $k(\omega)$ ,  $\sigma(\omega)$  and  $\alpha(\omega)$  spectra by Kramers–Kronig transformations between  $\epsilon_1(\omega)$  and  $\epsilon_2(\omega)$  [Eqs. SQ3 and SQ4], between  $n(\omega)$  and  $k(\omega)$  [Eqs. SQ6 and SQ7] as well as Eqs. SQ11 and SQ13, respectively.



**Table 7** Calculated critical points in the  $\epsilon_2(\omega)$ ,  $k(\omega)$ ,  $\sigma(\omega)$  and  $\alpha(\omega)$  spectra of binary, ternary and quaternary specimens within  $Mg_xZn_{1-x}Se_yTe_{1-y}$  alloys using mBJ and EV-GGA functional

x	y	Specimen	Critical point (eV) in the spectra of							
			$\epsilon_2(\omega)$		$k(\omega)$		$\sigma(\omega)$		$\alpha(\omega)$	
			mBJ	EV-GGA	mBJ	EV-GGA	mBJ	EV-GGA	mBJ	EV-GGA
0.0	0.0	ZnTe	2.455	1.884	3.252	1.803	3.163	2.456	3.136	2.564
	0.25	ZnSe <sub>0.25</sub> Te <sub>0.75</sub>	2.537	1.911	3.278	1.884	3.212	2.483	3.163	2.592
	0.50	ZnSe <sub>0.50</sub> Te <sub>0.50</sub>	2.809	2.102	3.387	1.993	3.325	2.565	3.299	2.646
	0.75	ZnSe <sub>0.75</sub> Te <sub>0.25</sub>	3.027	2.292	3.415	2.183	3.432	2.637	3.408	2.755
	1.0	ZnSe	3.326	2.486	3.445	2.537	3.626	2.782	3.598	2.837
0.25	0.0	Mg <sub>0.25</sub> Zn <sub>0.75</sub> Te	2.619	2.048	3.306	1.993	3.192	2.564	3.218	2.673
	0.25	Mg <sub>0.25</sub> Zn <sub>0.75</sub> Se <sub>0.25</sub> Te <sub>0.75</sub>	2.782	2.184	3.388	2.075	3.272	2.646	3.272	2.755
	0.50	Mg <sub>0.25</sub> Zn <sub>0.75</sub> Se <sub>0.50</sub> Te <sub>0.50</sub>	3.001	2.237	3.555	2.211	3.408	2.728	3.408	2.809
	0.75	Mg <sub>0.25</sub> Zn <sub>0.75</sub> Se <sub>0.75</sub> Te <sub>0.25</sub>	3.272	2.591	3.768	2.591	3.571	2.891	3.573	2.945
	1.0	Mg <sub>0.25</sub> Zn <sub>0.75</sub> Se	3.571	2.837	3.903	2.863	3.789	3.054	3.778	3.109
0.50	0.0	Mg <sub>0.50</sub> Zn <sub>0.50</sub> Te	2.809	2.299	3.333	2.183	3.274	2.728	3.326	2.809
	0.25	Mg <sub>0.50</sub> Zn <sub>0.50</sub> Se <sub>0.25</sub> Te <sub>0.75</sub>	3.001	2.455	3.415	2.483	3.385	2.918	3.435	2.945
	0.50	Mg <sub>0.50</sub> Zn <sub>0.50</sub> Se <sub>0.50</sub> Te <sub>0.50</sub>	3.244	2.646	3.578	2.619	3.544	3.054	3.598	3.082
	0.75	Mg <sub>0.50</sub> Zn <sub>0.50</sub> Se <sub>0.75</sub> Te <sub>0.25</sub>	3.489	2.863	3.838	2.836	3.734	3.190	3.761	3.190
	1.0	Mg <sub>0.50</sub> Zn <sub>0.50</sub> Se	3.816	3.183	3.987	3.244	3.972	3.299	3.979	3.300
0.75	0.0	Mg <sub>0.75</sub> Zn <sub>0.25</sub> Te	3.109	2.637	3.361	2.483	3.461	2.946	3.489	3.000
	0.25	Mg <sub>0.75</sub> Zn <sub>0.25</sub> Se <sub>0.25</sub> Te <sub>0.75</sub>	3.299	2.954	3.442	2.639	3.598	3.190	3.626	3.190
	0.50	Mg <sub>0.75</sub> Zn <sub>0.25</sub> Se <sub>0.50</sub> Te <sub>0.50</sub>	3.517	3.000	3.605	2.809	3.762	3.263	3.789	3.217
	0.75	Mg <sub>0.75</sub> Zn <sub>0.25</sub> Se <sub>0.75</sub> Te <sub>0.25</sub>	3.843	3.245	3.874	3.054	4.007	3.354	4.007	3.408
	1.0	Mg <sub>0.75</sub> Zn <sub>0.25</sub> Se	4.143	3.544	4.046	3.251	4.251	3.597	4.224	3.571
1.0	0.00	MgTe	3.789	3.462	3.986	3.217	4.143	3.517	3.982	3.598
							3.57 <sup>a</sup>			
	0.25	MgSe <sub>0.25</sub> Te <sub>0.75</sub>	3.925	3.598	4.122	3.326	4.224	3.625	4.061	3.680
	0.50	MgSe <sub>0.50</sub> Te <sub>0.50</sub>	4.172	3.816	4.235	3.544	4.387	3.762	4.224	3.789
	0.75	MgSe <sub>0.75</sub> Te <sub>0.25</sub>	4.415	4.034	4.313	3.789	4.578	3.925	4.415	3.925
	1.0	MgSe	4.744	4.170	4.421	4.115	4.853	4.061	4.659	4.034
			4.58 <sup>a</sup>				4.74 <sup>a</sup>			

Earlier theoretical data: <sup>a</sup>Ref. [77]

### 3.4 Selection of substrates for the growth of quaternary alloys

In this section, we have investigated the possibility of lattice matching between  $Mg_xZn_{1-x}Se_yTe_{1-y}$  and ZnTe and InAs in order to test their acceptability as appropriate substrate for the growth of these quaternary alloys and adopt some knowledge about interfaces of our investigated alloys and immediacy effects on them. This is due to the fact that their lattice constants and lattice constants of some of these quaternary alloys are very close. With zinc-blende crystal structure, ZnTe and InAs are also direct band gap semiconductors. Therefore, they can be chosen as suitable substrates for the growth of some of the  $Mg_xZn_{1-x}Se_yTe_{1-y}$  alloys. The lattice parameter of ZnTe and InAs are found experimentally as 6.08 Å and 6.058 Å, respectively.

The lattice constant  $a(x, y)$  for the quaternary alloy is determined using the modified Vegard’s rule as [104]:

$$a(x, y) = xy a_{MgSe} + (1 - x)y a_{ZnSe} + x(1 - y)a_{MgTe} + (1 - x)(1 - y)a_{ZnTe} \tag{10}$$

Here,  $a_{MgSe}$ ,  $a_{MgTe}$ ,  $a_{ZnSe}$  and  $a_{ZnTe}$  are the lattice constants of MgSe, MgTe, ZnSe and ZnTe, respectively.

Now, substituting the  $a(x, y)$  with the lattice constant of ZnTe in Eq. 10, the condition for lattice matching of  $Mg_xZn_{1-x}Se_yTe_{1-y}$  is

$$y = \frac{0.3345x + 0.1025}{0.0735x + 0.4485} \quad (0 \leq x \leq 1) \tag{11}$$

Similarly, the condition for lattice matching of  $Mg_xZn_{1-x}Se_yTe_{1-y}$  with InAs, obtained by substituting the  $a(x, y)$  with the lattice constant of InAs in Eq. 10, is

$$y = \frac{0.3345x + 0.1245}{0.0735x + 0.4485} \quad (0 \leq x \leq 1) \quad (12)$$

In this study, we have seen that six quaternaries achieve less than 5% as lattice mismatching to ZnTe substrate. These quaternaries correspond to specific concentrations  $x=0.25$ ,  $y=0.25$ ;  $x=0.50$ ,  $y=0.25$ ;  $x=0.50$ ,  $y=0.50$ ;  $x=0.75$ ,  $y=0.25$ ;  $x=0.75$ ,  $y=0.50$ ;  $x=0.75$ ,  $y=0.75$  and the lattice mismatching values are 1.59%, 2.90%, 1.003%, 0.411%, 2.20% and 0.03%, respectively. On the other hand, there are seven quaternary alloys, which achieve less than 5% as a lattice mismatching to InAs substrate. They correspond to specific concentrations  $x=0.25$ ,  $y=0.25$ ;  $x=0.25$ ,  $y=0.50$ ;  $x=0.50$ ,  $y=0.25$ ;  $x=0.50$ ,  $y=0.50$ ;  $x=0.75$ ,  $y=0.25$ ;  $x=0.75$ ,  $y=0.50$ ;  $x=0.75$ ,  $y=0.75$  and the lattice mismatching values are 1.90%, 0.09%, 3.20%, 1.37%, 4.50%, 2.57% and 0.39%, respectively.

Each of the Eqs. 11 and 12 provides a line of  $x$  and  $y$  concentrations in which the corresponding alloys are lattice matched to ZnTe and InAs, respectively. We have considered three different concentrations along the straight line (0.25, 0.398); (0.50, 0.556); (0.75, 0.702) for ZnTe substrate and (0.25, 0.447); (0.50, 0.601); (0.75, 0.746) for InAs substrate. In Figs. 10 and 11, the EVGGA and TB-mBJ based calculated energy band gaps as a function of magnesium ( $x$ ) concentration along the ZnTe and InAs matching line, respectively, in the composition plane are presented. The results show that one can tune the cationic ( $x$ ) and anionic ( $y$ ) concentrations in quaternary alloys to achieve a wide range of band gaps and hence the optical properties for alloys grown on each of the ZnTe and InAs substrate. It is clear from Fig. 10 that the band gap ranges from 2.30 to 3.25 eV with EV-GGA functional and from 2.94 to 3.98 eV with mBJ functional in case of ZnTe substrate. On the other hand, it is found from Fig. 11 that in case of InAs substrate, the band gap ranges from 2.35 to 3.35 eV with EV-GGA functional and from 3.00 to 4.08 eV with mBJ functional.

#### 4 Comments on accuracy of the calculated results

The compounds under the quaternary system  $\text{Mg}_x\text{Zn}_{1-x}\text{Se}_y\text{Te}_{1-y}$  are generated by combining four binary compounds ZnSe, ZnTe, MgSe and MgTe in different cationic ( $x$ ) and anionic ( $y$ ) concentrations. In our calculations, we have observed that the calculated lattice constants, bulk modulus, electronic band gaps and several optical constants of these source/parent binary compounds agree excellently well with the corresponding experimental data. In case of ternary or quaternary specimens, though no such experimental data are available, the calculated aforesaid parameters with different employed exchange–correlation functional

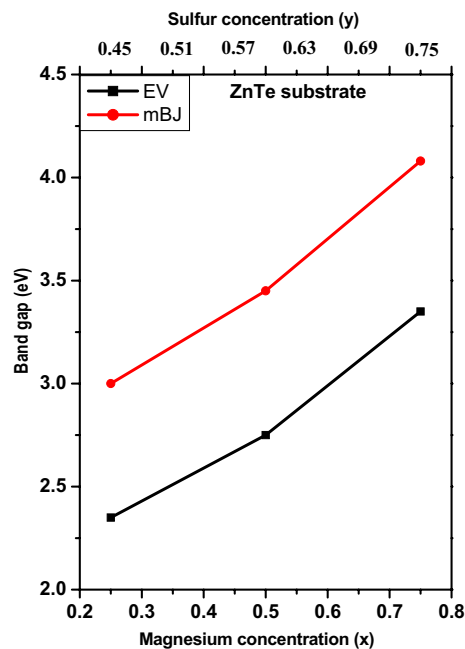


**Fig. 10** Energy band gap of  $\text{Mg}_x\text{Zn}_{1-x}\text{Se}_y\text{Te}_{1-y}$  quaternary alloys lattice matched to ZnTe as a function of Mg-concentration  $x$  mBJ (red line) and EVGGA (black line) functional

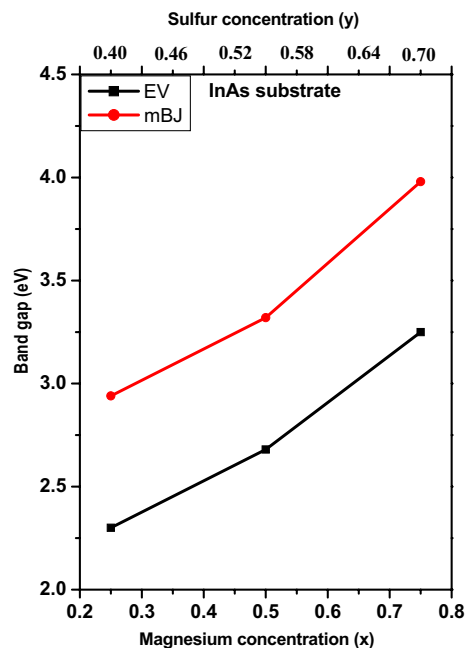


**Fig. 11** Energy band gap of  $\text{Mg}_x\text{Zn}_{1-x}\text{Se}_y\text{Te}_{1-y}$  quaternary alloys lattice matched to InAs as a function of Mg-concentration  $x$  mBJ (red line) and EVGGA (black line) functional

are according to our expectations and can be explained from the point of view of physics. Again, we have observed that variations of aforesaid parameters with  $x$  and  $y$  are in

accordance with the established physical laws and they have been explained in different sections of the manuscript. For example, well known Penn model states that semiconductor with lower band gap possesses higher  $\epsilon_1(0)$  and vice versa. Variation of our calculated  $\epsilon_1(0)$  with band gap satisfies the Penn model in an excellent manner. In case of other calculated parameters, nature of their concentration dependences also shows very good correlation with respective established physical law(s). Since the calculated results on different parameters for source/parent binaries show excellent matching with corresponding experiments and their natures of variations with cationic and anionic concentrations are in accordance with different well-established physical laws, our calculations have presented reliable results on different aspects of the concerned specimens with high degree of accuracy according to our opinion.

## 5 Conclusion

DFT-based FP-LAPW approach in combination with PBE-GGA, EV-GGA and mBJ functional has been employed to calculate the structural and optoelectronic properties of the specimens within  $\text{Mg}_x\text{Zn}_{1-x}\text{Se}_y\text{Te}_{1-y}$  quaternary system as a function of the compositions  $x$  and  $y$ . Considering the whole range of anionic concentrations ( $y$ ) at each of the fixed cationic concentrations ( $x$ ) and vice versa, the  $\text{Mg}_x\text{Zn}_{1-x}\text{Se}_y\text{Te}_{1-y}$  quaternary system has been divided into five binary-ternary and ternary-quaternary sub-systems in each category and elaborate studies have been made on the concentration dependences of the said properties. Concentration  $x$  and  $y$  dependence of the lattice constant, bulk modulus and band gap exhibits nonlinear behavior. At each of the cationic (Mg) concentrations,  $x$ , the lattice constant decreases, while the bulk modulus increases with increase in anionic (Se) concentration  $y$ . On the other hand, we have observed increase in lattice constant and decrease in bulk modulus with increase in cationic concentration  $x$  at each of the fixed anionic concentrations  $y$ . The direct band gap ( $\Gamma$ - $\Gamma$ ) is observed in each of the specimens within  $\text{Mg}_x\text{Zn}_{1-x}\text{Se}_y\text{Te}_{1-y}$  quaternary system. At each of the cationic concentrations  $x$ , band gap increases with increase in anionic concentrations  $y$  and similar trend is observed in case of variation of band gap with cationic concentrations  $x$  at each of the anionic concentrations  $y$ . Frequency responses of different optical parameters have been computed. It is observed that the zero-frequency limit in each of the  $\epsilon_1(\omega)$ ,  $n(\omega)$  and  $R(\omega)$  spectra shows opposite trend, while the critical points in each of the  $\epsilon_2(\omega)$ ,  $k(\omega)$ ,  $\sigma(\omega)$  and  $\alpha(\omega)$  spectra show the same trend of variation of band gap with concentrations  $x$  and  $y$ . Finally, the lattice matching of  $\text{Mg}_x\text{Zn}_{1-x}\text{Se}_y\text{Te}_{1-y}$  quaternary alloys to ZnTe and InAs substrates has been calculated and found that these substrates are suitable for the growth of some of

the said quaternary alloys. The results on the quaternary alloys should be useful for designing optoelectronic devices in the visible and UV spectral range, when they are lattice matched to ZnTe and InAs substrates.

## References

1. D. Long, J.L. Schmit, *Semiconductors and Semimetals* (Academic Press, New York, 1970)
2. C. Chauvet, V. Bousquet, E. Tournie, J.P. Faurie, J. Electronic Mater. **28**, 662 (1999)
3. S. Adachi, *Properties of Group-IV, III-V and II-VI Semiconductors* (John Wiley, New York, 2005)
4. J. Wang, M. Isshiki, *Wide-Band-gap II-VI Semiconductors: Growth and properties Springer Handbook of Electronic and Photonic Materials* (Springer, Berlin, 2006)
5. C.G. Van de Walle, *Wide-Band-Gap Semiconductors* (North Holland, Amsterdam, 1993)
6. V. Tomashyk, P. Feychuk, L. Shcherbak, *Ternary Alloys Based on II-VI Semiconductor Compounds* (CRC Press, New York, 2014)
7. V. Tomashyk, *Quaternary Alloys Based on II-VI Semiconductor Compounds* (CRC Press, New York, 2015)
8. S. Adachi, *Properties of Semiconductor Alloys* (Wiley, UK, 2009)
9. M.A. Hasse, J. Qui, J.M. De Puydt, H. Cheng, Appl. Phys. Lett. **59**, 1272–1274 (1991)
10. H.P. Wagner, S. Wittmann, H. Schmitzer, H. Stanzl, J. Appl. Phys. **77**, 3637–3640 (1995)
11. M.C. Tamargo, M.J.S.P. Brasil, R.E. Nahory, R.J. Martin, A.L. Weaver, H.L. Gilchrist, Semicond. Sci. Technol. **6**, A8–A13 (1991)
12. M.W. Wang, J.F. Swenberg, M.C. Phillips, E.T. Yu, J.O. McCaldin, Appl. Phys. Lett. **64**, 3455–3457 (1994)
13. R.J. Nelmes, M.I. McMohan, Semicond. Semimetals **54**, 145–246 (1998)
14. R.G. Greene, H. Luo, A.L. Ruoff, J. Phys. Chem. Solids **56**, 521–524 (1995)
15. S. Ves, *Band Gaps and Phase Transitions in Cubic ZnS, ZnSe and ZnTe*. In: H. D. Hochheimer, R. D. Eters (eds) *Frontiers of High-Pressure Research. NATO ASI Series (Series B: Physics)*, vol 286. (Springer, Boston, 1991).
16. A. San-Miguel, A. Polian, M. Gauthier, J.P. Itie, Phys. Rev. B **48**, 8683–8693 (1993)
17. A.L. Ruoff, T. Li, A.C. Ho, M.F. Pai, H. Luo, R.G. Greene, C. Narayana, J.C. Molstad, S.S. Trail, F.J. DiSalvo, P.E. Van Camp, Phys. Rev. Lett. **81**, 2723–2726 (1998)
18. T. Li, H. Luo, R.G. Greene, A.L. Ruoff, S.S. Trail, F.J. DiSalvo Jr., Phys. Rev. Lett. **74**, 5232–5235 (1995)
19. H. Okuyama, K. Nakano, T. Miyajima, K. Akimoto, J. Cryst. Growth **117**, 139–143 (1992)
20. O. Medelung (ed.), *Landolt Bornstein: Numerical Data and Functional Relationship in Science and Technology*, vol. 17b (Springer, Berlin, 1982)
21. NKh Abrikosov, V.B. Bankina, L.V. Poretskaya, L.E. Shelimova, E.V. Skudnova, *Semiconducting II-VI(IVVI and V-VI Compounds* (Plenum, New York, 1969)
22. W.H. Strehlow, E.L. Cook, J. Phys. Chem. Ref. Data **2**, 163–199 (1973)
23. W.A. Harrison, *Electronic Structure and the Properties of Solids* (Freeman, San-Francisco, 1980)
24. H. Okuyama, K. Nakano, T. Miyajima, K. Akimoto, Japanese. J. Appl. Phys. **30**, L1620–L1623 (1991)

25. A. Manabe, A. Mitsuishi, H. Yoshinaga, *Jpn. J. Appl. Phys.* **6**, 593–600 (1967)
26. D.T.F. Marple, *J. Appl. Phys.* **35**, 539–542 (1964)
27. B.H. Lee, *J. Appl. Phys.* **41**, 2988–2990 (1970)
28. D. Berlincourt, H. Jaffe, L.R. Shiozawa, *Phys. Rev.* **29**, 1009–1017 (1963)
29. B. Jobst, D. Hommel, U. Lunz, T. Gerhard, G. Landwehr, *Appl. Phys. Letts.* **69**, 97–99 (1996)
30. K. Watanabe, MTh Litz, M. Korn, W. Ossau, A. Waag, G. Landwehr, U. Schussler, *J. Appl. Phys.* **81**, 451–455 (1997)
31. T. Asano, K. Funato, F. Nakamura, A. Ishibashi, *J. Cryst. Growth* **156**, 373–376 (1995)
32. MTh Litz, K. Watanabe, M. Korn, H. Ress, U. Lunz, W. Ossau, A. Waag, G. Landwehr, Th Walter, B. Neubauer, D. Gerthsen, U. Schussler, *J. Cryst. Growth* **159**, 54–57 (1996)
33. A.U. Ubale, Y.S. Sakhare, S.G. Ibrahim, M.R. Belkhedkar, *Solid State Sci.* **23**, 96–101 (2013)
34. A.U. Ubale, Y.S. Sakhare, *Materi. Sci. Semicond. Process.* **16**, 1769–1774 (2013)
35. R. Dahmani, L. Salamanca-Riba, N.V. Nguyen, D. Chandler-Horowitz, B.T. Jonker, *J. Appl. Phys.* **76**, 514–517 (1994)
36. Y.D. Kim, S.L. Cooper, M.V. Klein, *Appl. Phys. Lett.* **62**, 2387–2389 (1993)
37. J.S. Kim, S.H. Suh, C.H. Kim, S.J. Chung, *J. Appl. Phys.* **81**, 6107–6111 (1997)
38. A. Waag, H. Heinke, S. Scholl, C.R. Becker, G. Landwehr, *J. Cryst. Growth* **131**, 607–611 (1993)
39. R.C. Tu, Y.K. Su, C.F. Li, Y.S. Huang, S.T. Chou, W.H. Lan, S.L. Tu, H. Chang, *J. Appl. Phys.* **83**, 1664–1669 (1998)
40. C.H. Hsu, C.Y. Yan, W.H. Kao, Y.T. Yu, H.H. Tung, *Ferroelectrics* **491**, 118–126 (2016)
41. J. Camacho, A. Cantarero, I. Hernández-Calderon, L. Gonzalez, *J. Appl. Phys.* **92**, 6014–6018 (2002)
42. Y. Yang, Y. Hu, C. Liu, W. Li, J. Zhang, L. Wu, J. Yang, *Chalcogenide Lett.* **13**, 521–528 (2016)
43. E. M. Larramendi, K. Gutierrez Z-B, C. Arens, U. Woggon, D. Schikora, K. Lischka, *J. Appl. Phys.* **107**, 103510–103514 (2010)
44. F. Xu, B. Xue, F. Wang, A. Dong, *Chem. Mater.* **27**, 1140–1146 (2015)
45. H. Lee, In-Young. Kim, J. Powell, D. E. Aspnes, S. Lee, F. Peiris, J. K. Furdyna, *J. Appl. Phys.* **88**, 878–882 (2000)
46. F. Firszt, S. Legowski, H. Męczyńska, H.L. Oczkowski, W. Osinska, J. Szatkowski, W. Paszkowicz, Z.M. Spolnik, *J. Cryst. Growth* **159**, 167–170 (1996)
47. K.J. Kim, M.H. Lee, J.H. Bahng, C.Y. Kwak, E. Oh, *Solid State Commun.* **105**, 17–20 (1998)
48. X. Liu, U. Bindley, Y. Sasaki, J.K. Furdyna, *J. Appl. Phys.* **91**, 2859–2865 (2002)
49. K. Naniwae, H. Iwata, K. Yashiki, *Appl. Phys. Letts.* **74**, 3984–3986 (1999)
50. J.H. Chang, H.M. Wang, M.W. Cho, H. Makino, H. Hanada, T. Yao, K. Shim, H. Rabitz, *J. Vacuum Sci. Techn. B* **18**, 1530–1533 (2000)
51. S.H. Wei, A. Zunger, *Phys. Rev. B* **37**, 8958–8981 (1988)
52. O. Zakharov, A. Rubio, X. Blase, M.L. Cohen, S.G. Louie, *Phys. Rev. B* **50**, 10780–10787 (1994)
53. A.E. Merad, M.B. Kanoun, J. Cibert, H. Aourag, G. Merad, *Phys. Lett. A* **315**, 143–149 (2003)
54. X.J. Chen, A. Mintz, J.S. Hu, X.L. Hua, J. Zinck, W.A. Goddard-III, *J. Vac. Sci. Technol. B* **13**, 1715–1727 (1995)
55. N.E. Christensen, O.B. Christensen, *Phys. Rev. B* **33**, 4739–4746 (1986)
56. G.D. Lee, M.H. Lee, J. Ihm, *Phys. Rev. B* **52**, 1459–1462 (1995)
57. R.A. Casali, N.E. Christensen, *Solid State Commun.* **108**, 793–798 (1998)
58. R. Gangadharan, V. Jayalakshmi, J. Kalaiselvi, S. Mohan, R. Murugan, B. Palanivel, *J. Alloy. Compd.* **359**, 22–26 (2003)
59. R. Khenata, A. Bouhemadou, M. Sahnoun, A.H. Reshak, H. Baltache, M. Rabah, *Comput. Mater. Sci.* **38**, 29–38 (2006)
60. M. Bilal, M. Shafiq, I. Ahmad, I. Khan, *J. Semicond.* **35**, 072001–072009 (2014)
61. F. Kootstra, P.L. de Boeij, J.G. Snijders, *Phys. Rev. B* **62**, 7071–7083 (2000)
62. H.Y. Wang, J. Cao, X.Y. Huang, J.M. Huang, *Condensed Matter Phys.* **15**, 13705–13714 (2012)
63. J. Heyd, J.E. Peralta, G.E. Scuseria, *J. Chem. Phys.* **123**, 174101–174107 (2005)
64. P.E. Van Camp, V.E.V. Doren, J.L. Martins, *Phys. Rev. B* **55**, 775–779 (1997)
65. F. Drief, A. Tadjer, D. Mesri, H. Aourag, *Catal. Today* **89**, 343–355 (2004)
66. S. Duman, S. Bagci, H.M. Tutuncu, G.P. Srivastava, *Phys. Rev. B* **73**, 205201–205214 (2006)
67. G. Gokoglu, M. Durandurdu, O. Gulseren, *Comp. Mater. Sci.* **47**, 593–598 (2009)
68. D. Rached, N. Benkhetto, B. Soudini, B. Abbar, N. Sekkal, M. Driz, *Phys. Status Solidi B* **240**, 565–573 (2003)
69. G. Kalpana, B. Palanivel, R.M. Thomas, M. Rajagopalan, *Phys. B* **222**, 223–228 (1996)
70. S. G. Lee, K. J. Chang, *Phys. Rev. B* **52**, 1918–1925 (1995)
71. L. Tairi, S. Touam, A. Boumaza, M. Boukhtouta, H. Meradji, S. Ghemid, S. Bin Omran, F. El Haj Hassan, R. Khenata, *Phase Trans.*, **90**, 929–941 (2017)
72. A. Fleszar, W. Hanke, *Phys. Rev. B* **71**, 045207–045211 (2005)
73. J.E. Bernard, A. Zunger, *Phys. Rev. B* **34**, 5992–5996 (1986)
74. F. El Haj Hassan, B. Amrani, F. Bahsoun, *Phys. B* **391**, 363–370 (2007)
75. Y. Zhu, S.H. Zhang, X.Y. Zhang, A.M. Hao, S.L. Zhang, F. Yang, J.K. Yang, R.P. Liu, *Comput. Mater. Sci.* **50**, 2745–2749 (2011)
76. F. El Haj Hassan, B. Amrani, *J. Phys. Cond. Matter* **19**, 386234–386242 (2007)
77. A. Sajid, A. Afaq, G. Murtaza, *Chin. J. Phys.* **51**, 316–326 (2013)
78. Z. Charifi, H. Baaziz, N. Bouarissa, *Mater. Chem. Phys.* **84**, 273–278 (2004)
79. Z. Charifi, F. El Haj Hassan, H. Baaziz, Sh. Khosravizadeh, S. J. Hashemifar, H. Akbarzadeh, *J. Phys. Cond. Matter* **17**, 7077–7088 (2005)
80. N. Ullah, G. Murtaza, R. Khenata, J. Rehman, H. UdDin, S. Bin Omran, *Mater. Sci. Semicond. Proce.* **26**, 681–689 (2014)
81. I. Khan, F. Subhan, I. Ahmad, Z. Ali, *J. Phys. Chem. Solids* **83**, 75–84 (2015)
82. G. Murtaza, N. Ullah, A. Rauf, R. Khenata, S. Bin Omran, M. Sajjad, A. Waheed, *Mater. Sci. Semicond. Process.* **30**, 462–468 (2015)
83. N.A. Noor, A. Shaukat, *Int. J. Mod. Phys. B* **26**, 1250168–1250187 (2012)
84. K. Shim, H. Rabitz, J.H. Chang, T. Yao, *J. Crystal Growth* **214**(215), 350–354 (2000)
85. F. El Haj Hassan, S. J. Hashemifar, H. Akbarzadeh, *Phys. Rev. B* **73**, 195202–195207 (2006)
86. P. Hohenberg, W. Kohn, *Phys. Rev. B* **136**, 864–871 (1964)
87. W. Kohn, L.J. Sham, *Phys. Rev.* **140**, A1133–A1138 (1965)
88. O.K. Andersen, *Phys. Rev. B* **42**, 3063–3083 (1975)
89. P. Blaha, K. Schwarz, P. Sorantin, S.K. Trickey, *Comput. Phys. Commun.* **59**, 339–415 (1990)
90. P. Blaha, K. Schwarz, G. H. Madsen, D. Kvasnicka, J. Luitz, in: K. Schwarz (Ed.) *FP-LAPW+lo Program for Calculating Crystal Properties*, (Techn. WIEN2K, Austria, 2001).
91. J.P. Perdew, K. Burke, M. Ernzerhof, *Phys. Rev. Letts.* **77**, 3865–3868 (1996)

92. A.D. Becke, E.R. Johnson, *J. Chem. Phys.* **124**, 221101–221104 (2006)
93. F. Tran, P. Blaha, *Phys. Rev. Letts.* **102**, 226401–226404 (2009)
94. E. Engel, S.H. Vosko, *Phys. Rev. B* **47**, 13164–13174 (1993)
95. A. Kokalj, *Comp. Mat. Sci.* **28**, 155–168 (2003) (Code available from <https://www.xcrysden.org/>)
96. K. Hacini, H. Meradji, S. Ghemid, F. El Haj Hassan, *Chin. Phys. B* **21**, 036102–036108 (2012)
97. F.D. Murnaghan, *Proc. Natl. Acad. Sci. USA* **30**, 244–247 (1944)
98. L. Vegard, *Z. Phys.* **5**, 17–26 (1921)
99. J.P. Dismukes, L. Ekstrom, R.J. Paff, *J. Phys. Chem.* **68**, 3021–3027 (1964)
100. M. Fox, *Optical Properties of Solids* (Oxford University Press, UK, 2001)
101. C. Sifi, H. Meradji, M. Silmani, S. Labidi, S. Ghemid, E. B. Hanneche, F. El Haj Hassan, *J. Phys.: Cond. Mat.* **21**, 195401 (2009).
102. M. Dadsetani, A. Pourghazi, *Phys. Rev. B* **73**, 195102–195108 (2006)
103. D.R. Penn, *Phys. Rev.* **128**, 2093–2097 (1962)
104. H. Okuyama, Y. Kishita, A. Ishibashi, *Phys. Rev. B* **57**, 2257–2263 (1998)

**Publisher's Note** Springer Nature remains neutral with regard to jurisdictional claims in published maps and institutional affiliations.